

PL-TR-97-2150

Advances in Numerical Methods

K. L. McLaughlin

B. Shkoller

D. E. Wilkins

T. G. Barker

Maxwell Technologies
8888 Balboa Avenue
San Diego, CA 92123-1506

September 1997

19980421 120

Final Report

10 August 1995 – 9 August 1997

DTIC QUALITY INSPECTED 2

Approved for Public Release; Distribution Unlimited



U.S. DEPARTMENT OF ENERGY
Office of Nonproliferation and National Security
WASHINGTON, DC 20585



AIR FORCE RESEARCH LABORATORY
Space Vehicles Directorate
29 Randolph Road
AIR FORCE MATERIEL COMMAND
HANSCOM AFB, MA 0173103010

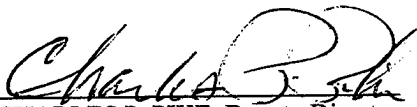
SPONSORED BY
Department of Energy
Office of Non-Proliferation and National Security

MONITORED BY
Air Force Research Laboratory
CONTRACT No. F19628-95-C-0207

The views and conclusions contained in this document are those of the authors and should not be interpreted as representing the official policies, either express or implied, of the Air Force or U.S. Government.

This technical report has been reviewed and is approved for publication.


KATHARINE KADINSKY-CADE
Contract Manager


CHARLES P. PIKE, Deputy Director
Integration and Operations Division

This report has been reviewed by the ESD Public Affairs Office (PA) and is releasable to the National Technical Information Service (NTIS).

Qualified requestors may obtain copies from the Defense Technical Information Center. All others should apply to the National Technical Information Service.

If your address has changed, or you wish to be removed from the mailing list, or if the addressee is no longer employed by your organization, please notify AFRL/VSOE, 29 Randolph Road, Hanscom AFB, MA 01731-3010. This will assist us in maintaining a current mailing list.

Do not return copies of the report unless contractual obligations or notices on a specific document requires that it be returned.

REPORT DOCUMENTATION PAGE			Form Approved OMB No. 0704-0188	
<small>Public reporting burden for this collection of information is estimated to average 1 hour per response, including the time for reviewing instructions, searching existing data sources, gathering and maintaining the data needed, and completing and reviewing the collection of information. Send comments regarding this burden estimate or any other aspect of this collection of information, including suggestions for reducing this burden, to Washington Headquarters Services, Directorate for Information Operations and Reports, 1215 Jefferson Davis Highway, Suite 1204, Arlington VA 22202-4302, and to the Office of Management and Budget, Paperwork Reduction Project (0704-0188), Washington, DC 20503.</small>				
1. AGENCY USE ONLY (Leave blank)	2. REPORT DATE September 1997	3. REPORT TYPE AND DATES COVERED Final - 08/10/95-08/09/97		
4. TITLE AND SUBTITLE Advances in Numerical Methods		5. FUNDING NUMBERS PE 69120H PR DENN TA GM WU AT F19628-95-C-0207		
6. AUTHOR(S) Keith L. McLaughlin D.E. Wilkins B. Shkoller T.G. Barker				
7. PERFORMING ORGANIZATION NAME(S) AND ADDRESS(ES) Maxwell Technologies 8888 Balboa Avenue San Diego, CA 92123-1506		8. PERFORMING ORGANIZATION REPORT NUMBER MFD-TR-97-15870		
9. SPONSORING/MONITORING AGENCY NAME(S) AND ADDRESS(ES) Air Force Research Laboratory 29 Randolph Road Hanscom AFB, MA 01731-3010 Contract Manager: Katherine Kadinsky-Cade/VSBS		10. SPONSORING/MONITORING AGENCY REPORT NUMBER PL-TR-97-2150		
11. SUPPLEMENTARY NOTES This research was sponsored by the Department of Energy, Office of Non-Proliferation and National Security, Washington, DC 20585.				
12a. DISTRIBUTION/AVAILABILITY STATEMENT Approved for public release; distribution unlimited.		12b. DISTRIBUTION CODE		
13. ABSTRACT (Maximum 200 words) This report summarizes work conducted over a two year period to improve numerical methods. The report has three main sections. Section 2 covers work on synthetics for layered earth models. Section 3 reports on three-dimensional (3D) elastic finite difference calculations and the relationship between one-dimensional (1D) (layered earth) and 3D laterally heterogeneous wavefields. Section 4 reports on development of a finite difference program to model the response of permeable hoses to atmospheric pressure fluctuations from wind turbulence.				
14. SUBJECT TERMS Synthetic Seismograms 3D Finite Differences Infrasound Permeable Hoses			15. NUMBER OF PAGES 64	
			16. PRICE CODE	
17. SECURITY CLASSIFICATION OF REPORT Unclassified	18. SECURITY CLASSIFICATION OF THIS PAGE Unclassified	19. SECURITY CLASSIFICATION OF ABSTRACT Unclassified	20. LIMITATION OF ABSTRACT SAR	

NSN 7540-01-280-5500

Standard Form 298 (Rev. 2-89)
Prescribed by ANSI Std. Z39-18
298-102

Unclassified

SECURITY CLASSIFICATION OF THIS PAGE

CLASSIFIED BY:

DECLASSIFY ON:

SECURITY CLASSIFICATION OF THIS PAGE

Unclassified

Table of Contents

1.0 Introduction.....	1
2.0 Layered Earth Model Wavenumber Integration Synthetics.....	2
2.1 Wavenumber Integration Synthetics Using A Parallel Virtual Machine.....	2
2.1.1 What is PVM?	2
2.1.2 Wavenumber Integration Synthesis -“The Perfect Parallel Algorithm”	3
2.2 Random Layering.....	5
2.3 Frequency Dependent Attenuation, $Q(f) = Q_0 * f^n$	11
2.4 Acknowledgments.....	16
2.5 References	16
3.0 Finite Difference 3D Regional Scattering Calculations.....	17
3.1 Introduction.....	17
3.2 Modal Spectra	24
3.3 Wavenumber Spectra	29
3.4 Conclusions	33
3.5 Acknowledgements.....	34
3.6 References	34
4.0 Permeable Hose Characteristics and Noise Reduction For Infrasound Monitoring.....	35
4.1 Summary	35
4.2 Introduction.....	35
4.3 Theory of Noise Reduction Hoses and Their Calibration	37
4.4 Analysis of a Helmholtz Oscillator.....	43
4.5 Finite Difference Modeling, Maxhose.....	44
4.6 Stability Conditions.....	48
4.7 Hose Calibration Simulation.....	49
4.8 Finite Difference Simulations of Wind Noise Response.....	49
4.9 Conclusions	52
4.10 Acknowledgments.....	53
4.11 References	53

List of Figures

1. The <i>master</i> program sends and receives messages through the PVM <i>daemon</i> (PVMD) which routes the messages to other <i>daemons</i> on the way to and from <i>slave</i> modules	4
2. Comparison of synthetic transverse component Green's function, G_{yxy} , at 400 km, source depth $h=15$ km, with (top) and without (below) 5% random velocity variations in the layered model D2	6
3. Comparison of vertical component Green's function, G_{zi} , at 400 km, source depth $h=1$ km, with (top) and without (below) 5% random velocity variations in the layered model D2	6
4. P-wave velocities versus depth for layered models DA, GA, H2, and N4 with 0%, 5%, 7.5%, and 10% velocity variations	7
5. Comparison of Green's functions for model DA with 0%, 2.5%, 5.0%, 7.5%, and 10% velocity variation (top to bottom)	8
6. Comparison of Green's functions for model GA with 0%, 2.5%, 5.0%, 7.5%, and 10% velocity variation (top to bottom)	8
7. Comparison of Green's functions for model H2 with 0%, 2.5%, 5.0%, 7.5%, and 10% velocity variation (top to bottom)	9
8. Comparison of Green's functions for model N4 with 0%, 2.5%, 5.0%, 7.5%, and 10% velocity variation (top to bottom)	9
9. Vertical seismogram at 600 km from an earthquake source ($h=12.5$ km) for layered model DA with 0%, 2.5%, 5.0%, 7.5%, and 10% velocity variation	10
10. Vertical component Lg/Pg ratio at 600 km from an earthquake source ($h=12.5$ km) for layered model DA with 0%, 2.5%, 5.0%, 7.5%, and 10% velocity variation.	10
11. Vertical component Lg/Pg spectral ratios for models DA, GA, H2, and N4 for an explosion source ($h=1$ km) and 0, 2.5, 5, 7.5, and 10% RMS random velocity layers	11
12. Compilation of average explosion Lg/Pg spectral ratios from Bennett <i>et al.</i> (1997) for explosions in Asia and Western US	13
13. Compilation of average Lg/Pg spectral ratios from Bennett <i>et al.</i> (1997) for earthquakes in Asia, Western US, and Eastern US	13
14. Comparison of vertical component synthetics (high pass at 0.5 Hz) at 200 km for three Q(f,z) models and velocity model D2, Q1 (top), Q2 (middle), Q3 (bottom)	14

15.	Comparison of vertical component synthetics (high pass at 0.5 Hz) at 200 km for three Q(f,z) models and velocity model D2, Q1 (top), Q2 (middle), Q3 (bottom).....	14
16.	Comparison of vertical component synthetics (high pass at 3.0 Hz) at 200 km for three Q(f,z) models and velocity model D2, Q1 (top), Q2 (middle), Q3 (bottom).....	15
17.	Comparison of vertical component synthetics (high pass at 3.0 Hz) at 200 km for three Q(f,z) models and velocity model D2, Q1 (top), Q2 (middle), Q3 (bottom).....	15
18.	Diagram of 3 levels of nested grids; 1 grid on level 1, 4 grids on level 2, and 16 grids on level 3 for a total of 21 grids. Each grid contains 64 x 64 x 128 = 524,288 cells for a total of 11 million cells	19
19.	Plot of the test structure used in all computations. P- and S-wave velocities in the crust are simple gradients with Poisson's ratio of 0.25	20
20.	Shear velocity along a Y = Constant slice of the model	20
21.	Visualization of the 3D random variation. Isosurfaces with absolute variation greater $\pm 1\sigma$ are shaded in the top image. Regions within $\pm 1\sigma$ are transparent.....	21
22.	Run #1 snap shots of vertical particle velocity on the Y = 0 plane, at T = 5 seconds.	22
23.	Run #1 snap shots of vertical particle velocity on the Y = 0 plane, at T = 10 seconds.	22
24.	Run #1 snap shots of vertical particle velocity on the Y = 0 plane, at T = 15 seconds.	22
25.	Run #1 snap shots of vertical particle velocity on the Y = 0 plane, at T = 20 seconds	23
26.	Run #1 snap shots of vertical particle velocity on the Y = 0 plane, at T = 25 seconds.	23
27.	Run #1 snap shots of vertical particle velocity on the Y = 0 plane, at T = 30 seconds.	23
28.	Comparison of finite difference and wavenumber integration synthetics for Run #1 (5% RMS, explosion source) at 100 km for lowpass filters 0.2, 0.4, 0.6, and 0.8 Hz (top to bottom)	24
29.	Plots of P-SV modes at 0.5 Hz (right) and 0.75 Hz (left) for the test structure shown in Figure 19	26
30.	Diagram of Modal Spectra. C(J,F). C(J,F) = 0 to the right of the modal cut-off line	26
31.	Modal spectra at 120 km (top) and 60 km (bottom) for models with 0% RMS (left) and 5% RMS (right) lateral heterogeneity.....	27

32.	Modal Spectral Ratio at 120 km 5% RMS model / 0% RMS model. Yellow and Red shades are modes enhanced w.r.t. the background model.....	28
33.	Ratio of 120 km to 60 km.....	28
34.	Diagram of wavenumber-wavenumber spectra at frequency, f	30
35.	Phase plane wavenumber impulse response for a cylindrical wave, 120 km from the source at 0.4 (left) and 0.6 Hz (right).....	30
36.	Phase plane wavenumber impulse response for an off-axis cylindrical wave, 120 km from the source at 0.6 Hz.....	31
37.	Wavenumber spectra of the vertical component velocity field on a $Y = 120$ km phase plane at 0.6 Hz for the 5% RMS (right) and 0% RMS (left).....	32
38.	Wavenumber spectra of the radial component velocity field on a $Y = 120$ km phase plane at 0.6 Hz for the 5% RMS (right) and 0% RMS (left).....	32
39.	Wavenumber spectra of the transverse component velocity field on a $Y = 120$ km phase plane at 0.6 Hz for the 5% RMS (right) and 0% RMS (left).....	33
40.	Contours of detection threshold in $\text{Log}(\text{Yield in Kt})$ at 90% probability for 2 infrasound detections at stations of the proposed IMS.....	36
41.	Contours of detection threshold in $\text{Log}(\text{Yield in Kt})$ at 90% probability for 3 infrasound detections at stations of the proposed.....	37
42.	Wind generated eddies create pressure fluctuations and hence noise.....	37
43.	A hose element: length dx , radius a , flow in the x direction q_x , flow in/out q_a	38
44.	A simple and inexpensive calibration configuration.....	40
45.	Shows rise time calibration of two 2.082 m long hoses.....	41
46.	A simple inexpensive diagnostic configuration.....	42
47.	Two short sections of 5/8" permeable hose were tested using the end-on test geometry described in the text.....	42
48.	Simple diagram of the principle part of a two ended Helmholtz oscillator.....	43
49.	A 0.32 m section of 5/8" non-permeable hose was set up as a Helmholtz oscillator and subjected to a 0.5 millibar step function change in pressure of one manifold.....	44
50.	Comparison of data and Maxhose finite difference simulation of the calibration test configuration of Figure 44.....	49

51.	Pressure variation in the hose as a function of time (seconds) and position (X in meters) for random white noise pressure fluctuations in the atmosphere	50
52.	RMS pressure fluctuations normalized to external atmospheric RMS fluctuations at the end of the hose and in the middle of the hose versus different hose lengths for a fixed characteristic length hose.....	50
53.	An atmospheric pressure history as a function of space and time on the left and the resulting pressure fluctuation signal in the hose on the right	51
54.	Pressure fluctuations inside and outside the middle of the hose simulation of Figure 53	52

List of Tables

1.	Computational Runs	19
----	--------------------------	----

1.0 Introduction

This report summarizes work conducted over a two year period to improve numerical methods. The report has three main sections. Section 2 covers work on synthetics for layered earth models. Section 3 reports on three-dimensional (3D) elastic finite difference calculations and the relationship between one-dimensional (1D) (layered earth) and 3D laterally heterogeneous wavefields. Section 4 reports on development of a finite difference program to model the response of permeable hoses to atmospheric pressure fluctuations from wind turbulence.

Section 2 reports on work conducted to port a wavenumber integration synthetics code to the Parallel Virtual Machine software and tests of this software. Numerical experiments were performed with random layering added to suites of layered crustal earth models. It was verified that random layering does make synthetics look more like observed seismograms without significantly altering the overall attenuation and spectra of Pg and Lg waveforms. The wavenumber integration code was modified to permit frequency dependent $Q(f)$ models. Numerous studies have found that Lg $Q(f)$ is proportional to frequency to some power ranging between 0 and 1. Such studies commonly parameterize $Q(f) = Q_0 * f^n$. Numerical experiments were performed with a suite of crustal models to compare synthetics with three different Q models.

In Section 3, we report on analysis of the 3D scattered wavefield computed using 3D elastic finite differences with modal summation and wavenumber spectra on phase screens. We compute scattered waves in randomly heterogeneous 3D velocity models. The total elastic wavefield (3 components of particle velocity) is saved on vertical planes at selected distances from the source. The modal spectra and wavenumber spectra is estimated on those planes and compared to computations for a layered structure in order to gain insight into the scattering process.

In Section 4, we report on development of a finite difference program, Maxhose, to compute the response of permeable hoses to atmospheric pressure fluctuations (noise) and signals. Permeable hose arrays are planned as noise reduction measures for the deployment of infrasound stations in the CTBT International Monitoring System. These noise reduction systems are critical to the expected performance of the entire infrasound system. Maxhose was developed to provide a useful tool for understanding and predicting the performance of hoses given the frequency-wavenumber characteristics of turbulent wind noise.

2.0 Layered Earth Model Wavenumber Integration Synthetics

2.1 Wavenumber Integration Synthetics Using A Parallel Virtual Machine

In the first year of this project a wavenumber integration program, *Prose* (Apsel and Luco, 1983), was ported from a single processor application to a parallel processing environment using the Parallel Virtual Machine (PVM) software environment. This software allows the user to harness a network of UNIX workstations to perform calculations in parallel. A PVM based parallel wavenumber integration program was developed that computes Green's functions in CSS 3.0 format readable with SAC. Near linear speed-up over a single processor has been realized with a heterogeneous network of SUN OS4/Solaris, HP, SGI, and DEC workstations tested over WAN and LAN. The software requires PVM 3.3.11, a FORTRAN F77 compiler, and a C compiler. The Gnu-make program is recommended on SGI, HP, and DEC workstations. Interested users should contact Keith L. McLaughlin (scatter@maxwell.com). Current information on the availability of the software can be found on the Internet at <http://www.maxwell.com/products/geop>. The interested reader is referred to McLaughlin and Shkoller (1996) for detailed descriptions of the load balancing algorithms employed.

2.1.1 What is PVM?

All parallel computer algorithms are composed of modules which are executed on multiple processors, messages that must be sent between these modules, and strategies for coordinating the modules and processors to work in parallel. The modules are typically distributed over a set of processors that are connected in some sort of communications network. Much of the programming work to develop a parallel algorithm is focused on passing messages between these modules and synchronizing their work. Commercially available massively parallel processors (MPP) provide custom compilers and libraries to facilitate this kind of programming. However, most research institutions already have the makings of a parallel machine; they typically have several workstations connected in a local area network. The aggregate computing power of their workstations often exceeds the CPU power that might be available at a supercomputer center. Furthermore, these machines are often idle much of the day or night.

Parallel Virtual Machine (PVM) is a public domain software system for turning a network of computers into a virtual parallel computer (Geist *et al.* 1994). The software supports heterogeneous networks including nearly all UNIX workstations and many parallel and single processor supercomputers. The software is based on widely used TCP/IP message passing protocols and therefore functions over a wide variety of local area networks (LAN) and wide area networks (WAN). The user interface libraries are both *FORTRAN* (F77 and F90) and *C* callable from a user's program. PVM frees the user from the arcane details of TCP/IP message passing between programs (processes) by providing a high level *C* or *FORTRAN* user interface and providing buffering and routing daemons for to the TCP/IP packets on the user's computer. This is done by running *daemon* process on each processor that serve as a relay posts for all messages passed between the user's programs running on each processor. PVM may be obtained by anonymous ftp from Oak Ridge National Lab and University of Tennessee at

http://www.epm.ornl.gov/pvm/pvm_home.html. Installation of PVM 3.3.11 requires an ANSI C compiler and can be accomplished in less than an hour.

2.1.2 Wavenumber Integration Synthesis -“The Perfect Parallel Algorithm”

Wavenumber integration calculations (Apsel and Luco, 1983) are computationally bound by the time it takes to compute the complex response between a source and a receiver for a given frequency. Wavenumber integration is also the “perfect parallel algorithm” because computation of one frequency 1) is independent of all other frequencies, 2) requires only a few input values, 3) results in only a few output values, and 4) there are many frequencies to compute. These programs are well suited to a *master - slave architecture* (Figure 1). The master program performs all file input/output and organizes the work of the many identical slave programs running on multiple processors in the network. We treat each slave program like a function call for each complex Green’s function response at a fixed frequency and fixed source and fixed receiver. Figure 2 illustrates the concept behind the use of the *master - slave* modules on a virtual parallel machine using PVM. The master program sends messages to the slave programs telling them which frequencies to compute and then waits for the results to return from the slaves in the form of messages. When the *slave* programs are not computing the response at a specific frequency, they are waiting for instructions from the *master* program. The *slave* programs return the numerical results as well as timing information that is useful in load balancing the calculation.

Parallel Virtual Machine

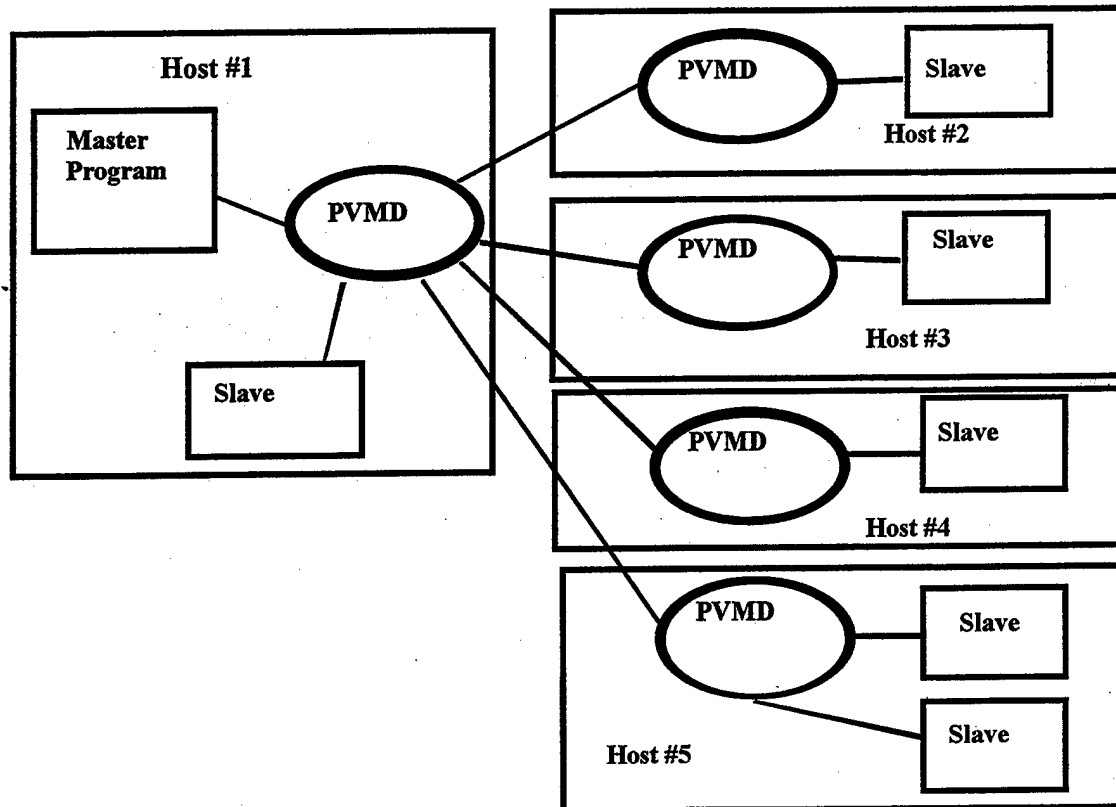


Figure 1. The *master* program sends and receives messages through the PVM *daemon* (PVMD) which routes the messages to other *daemons* on the way to and from *slave* modules. There may be multiple *slaves* on a single host and there is often both a *slave* and *master* program running on the same host.

Key to success is balancing the computational load between machines (hosts or processors) in the network. A heterogeneous network of workstations may contain a varied mix of slow and fast machines. Furthermore, as a computation proceeds, the load on each machine will change with time as other users start-up and terminate other processes. Also, some machines may be on a local network and communications may be almost instantaneous while others may be further away on a wide area network and messages may require a greater time for delivery. Therefore, it is necessary to keep a concise database within the master program of the relative performance of each processor. We use a very simple algorithm for load balancing; a list of processors is ranked by speed and a list of tasks (frequencies) is maintained. Tasks are checked off the list as they are completed and the next task is always sent to the fastest available host. Near the end of the computation, if we have sent each task out and we have available hosts, we do not wait for slow hosts to complete their tasks but rather re-send those tasks out to the fastest available host. The goal is to keep all slave modules working. The resulting algorithm is therefore robust with respect to changes that do happen in the network(s) and on the various parts of the parallel virtual machine. The reader is referred to McLaughlin and Shkoller (1996) for details.

The master and slave programs, *prosem* and *proses*, are based on the wavenumber integration algorithm of Apsel and Luco (1983). File formats and program options are discussed in the UNIX style manual page included with the software distribution. The master program, *prosem*, starts up the parallel virtual machine, spawns the slave programs, *proses*, on each host and saves the frequency domain output in a file. A second program, *gseis*, is then run that computes the time domain Green's functions and stores them in *CSS 3.0* format with a *wfdisc* file (see Anderson *et al.* 1990a and 1990b for definitions of *CSS 3.0* format). This seismogram format can be read and manipulated using a number of programs including the popular Seismic Analysis Code (*SAC*, 1995).

2.2 Random Layering

It has been suggested that introduction of random velocity variations into a layered crustal model produce more realistic looking regional phases (Harvey, 1992). Real regional seismograms tend to exhibit extended Pg and Lg wavetrains while layered Earth synthetics often have very simple regional waveforms consisting of several strong isolated spikes. One way to reduce these isolated spikes and generate more extended waveforms is to introduce interfaces that produce many small internal reflections between the up-going and down-going waves trapped in the crust. We have experimented with introducing 1 km thick layers and random velocities distributed about the mean background model. The modified Mooney *et al.* (1997) layered Earth models, and details of the synthetic computation procedures are described in Bennett *et al.* (1997), and the frequency and depth dependent attenuation model, $Q(f,z) = Q_0(\beta,z)f^n$, is described in Section 2.3 of this report. Figures 2 and 3 compare Green's functions model D2 with and without random layers of 5% variation. The Pn and Sn waveforms in the two sets of Green's functions are larger and more impulsive with the random layering than without. Also, some of the isolated spikes in the Pg and Lg wavetrains are reduced.

Figure 4 shows more such random perturbations to the DA, GA, H2, and N4 models of Mooney *et al.* (1997). Variations of 0%, 2.5%, 5%, 7.5%, and 10.0% RMS random velocity variation have been introduced into both P and S wave velocities throughout each model. Green's functions for these models are compared in Figure 5 through Figure 8. The four background models were chosen for their diversity; the models represent a thick set of platform deposits (DA), a high-velocity crust with very thin sediments (GA), a moderate velocity crust with no sediments (H2), and a thin crust with sediments (N4). Smoothed Lg/Pg spectral ratios computed from these synthetic seismograms are shown in Figure 11.

It is ironic that while our principal goal was to generate more realistic Pg and Lg waveforms, introduction of random layering has made the Pn and Sn waveforms larger, more impulsive, and more realistic. These waves travel in the upper mantle waveguide and are sensitive to the velocity gradients just below the Moho. The background mantle PEM model has no gradient except for the "earth flattening" approximation. We presume that in the absence of the many interfaces, the waves consist of only a few rays or modes that propagate in the upper mantle waveguide. Addition of the random interfaces appears to proliferate the number of rays/modes that contribute to the Pn and Sn waveforms.

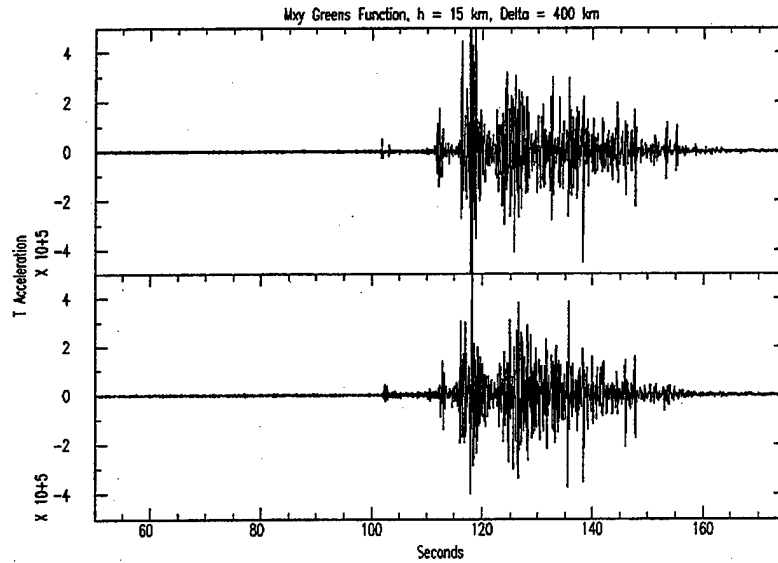


Figure 2. Comparison of synthetic transverse component Green's function, G_{yxy} , at 400 km, source depth $h=15\text{km}$, with (top) and without (below) 5% random velocity variations in the layered model D2. Note that the more impulsive Sn arrival from the random layered structure and that the reduced isolated "spikes" in the Lg signal.

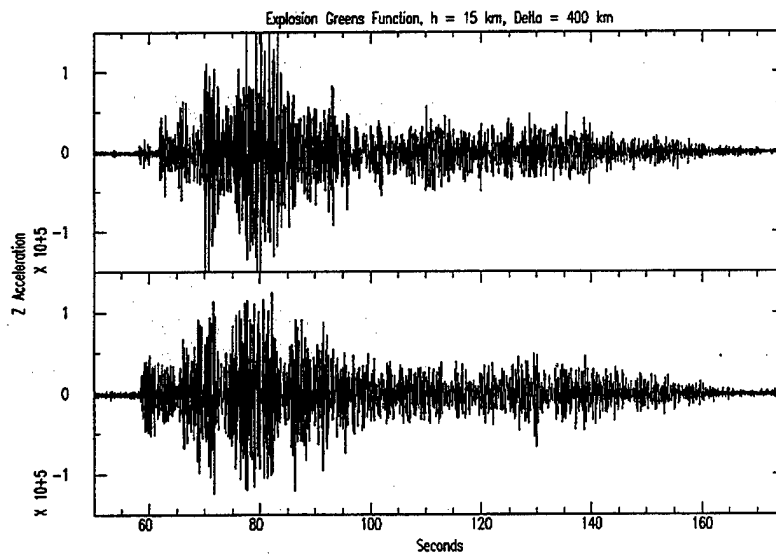


Figure 3. Comparison of vertical component Green's function, G_{zi} , at 400 km, source depth $h=1\text{km}$, with (top) and without (below) 5% random velocity variations in the layered model D2. Note the more impulsive Pn waveform and the reduced "spikes" in the Pg from the randomized structure.

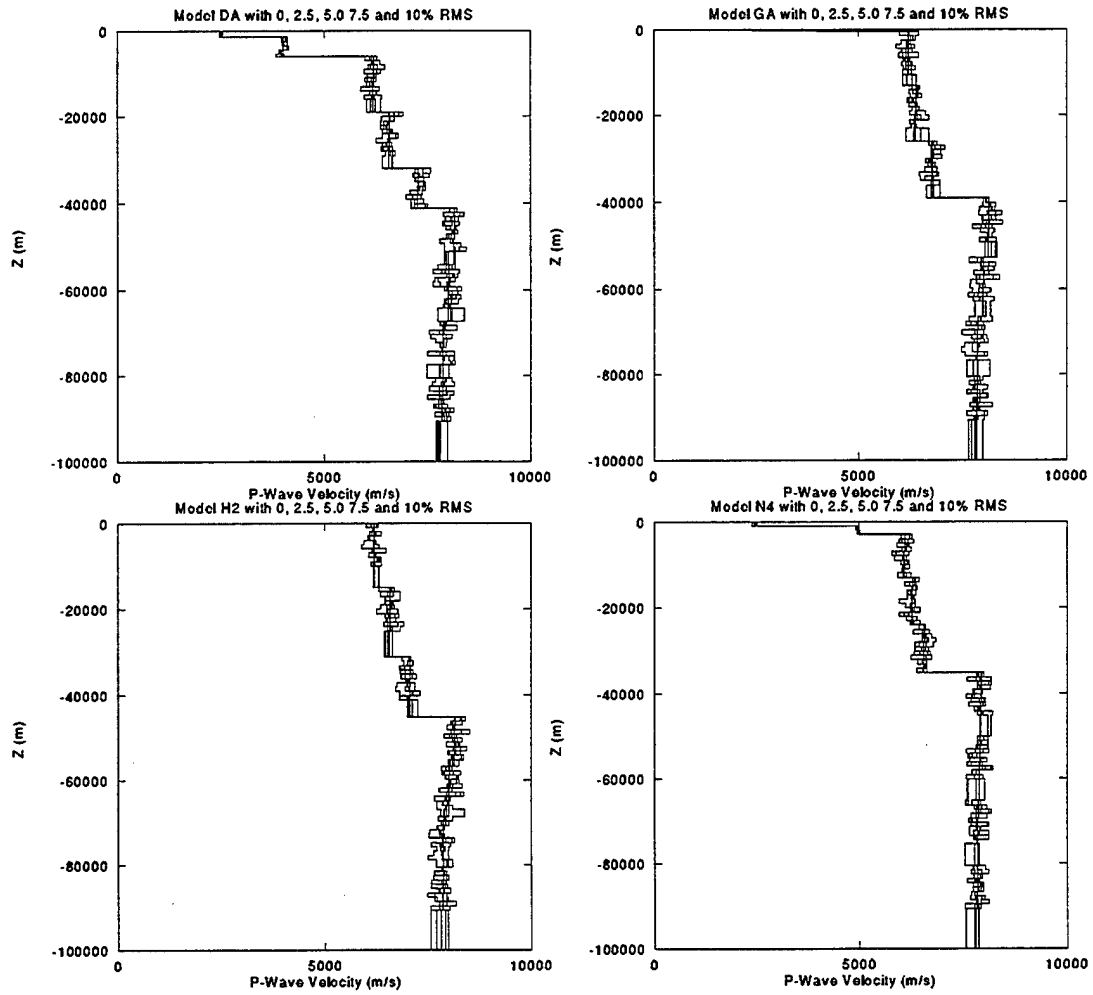


Figure 4. P-wave velocities versus depth for layered models DA, GA, H2, and N4 with 0%, 5%, 7.5%, and 10% velocity variations.

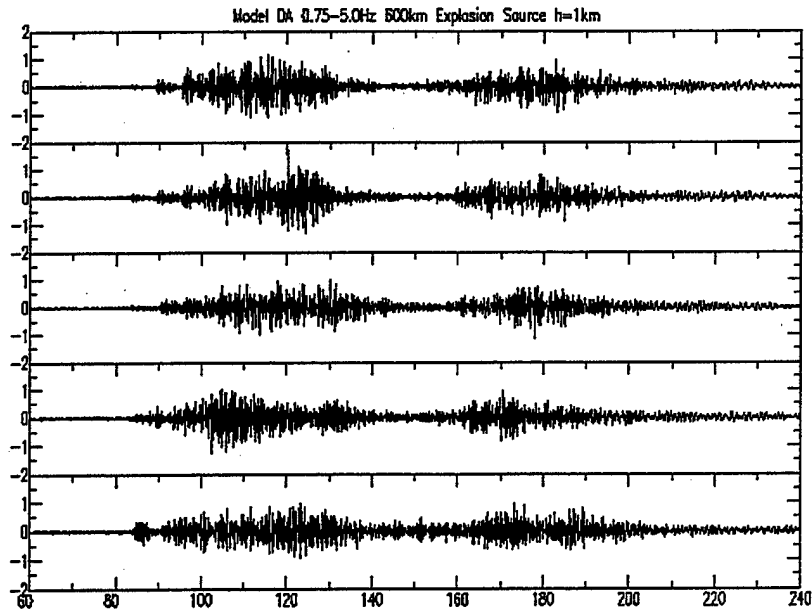


Figure 5. Comparison of Green's functions for model DA with 0%, 2.5%, 5.0%, 7.5%, and 10% velocity variation (top to bottom).

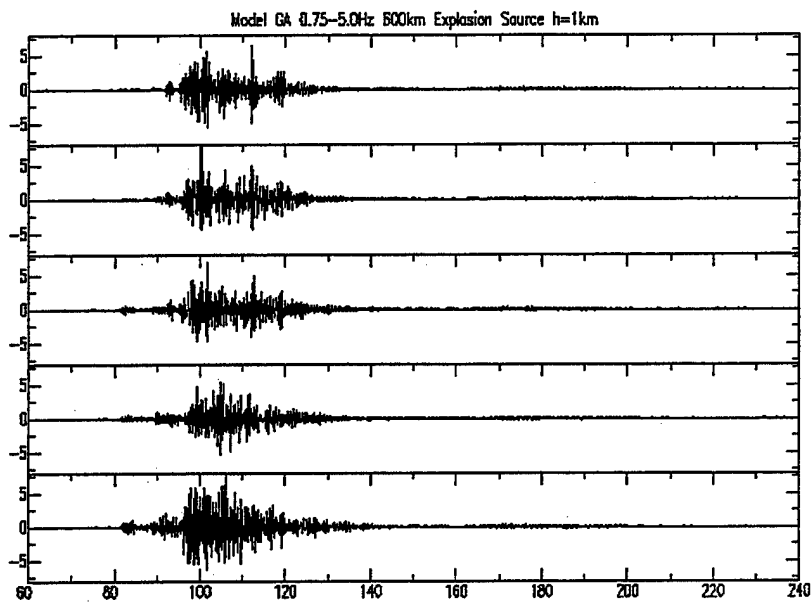


Figure 6. Comparison of Green's functions for model GA with 0%, 2.5%, 5.0%, 7.5%, and 10% velocity variation (top to bottom).

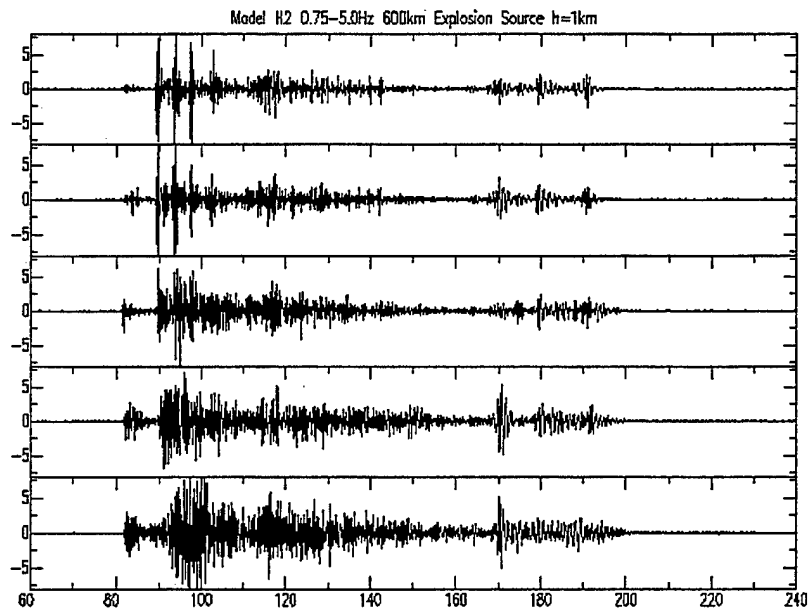


Figure 7. Comparison of Green's functions for model H2 with 0%, 2.5%, 5.0%, 7.5%, and 10% velocity variation (top to bottom).

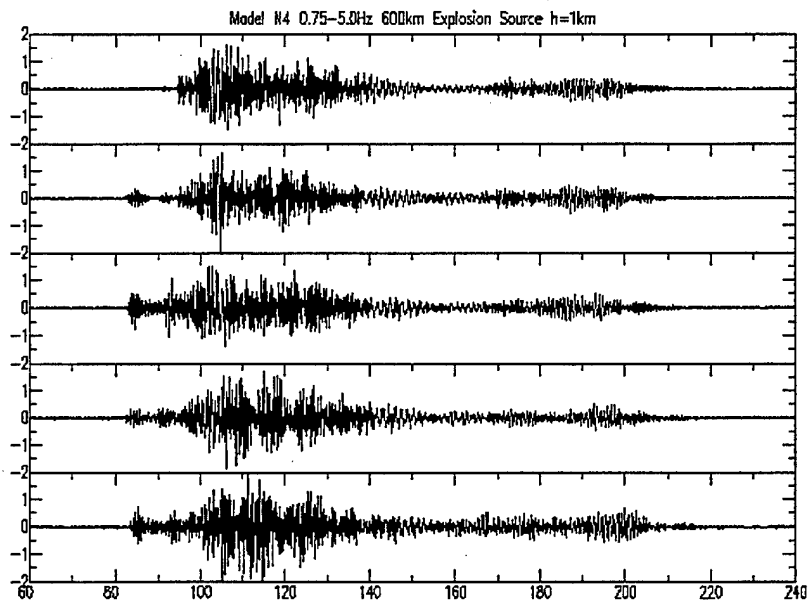


Figure 8. Comparison of Green's functions for model N4 with 0%, 2.5%, 5.0%, 7.5%, and 10% velocity variation (top to bottom).

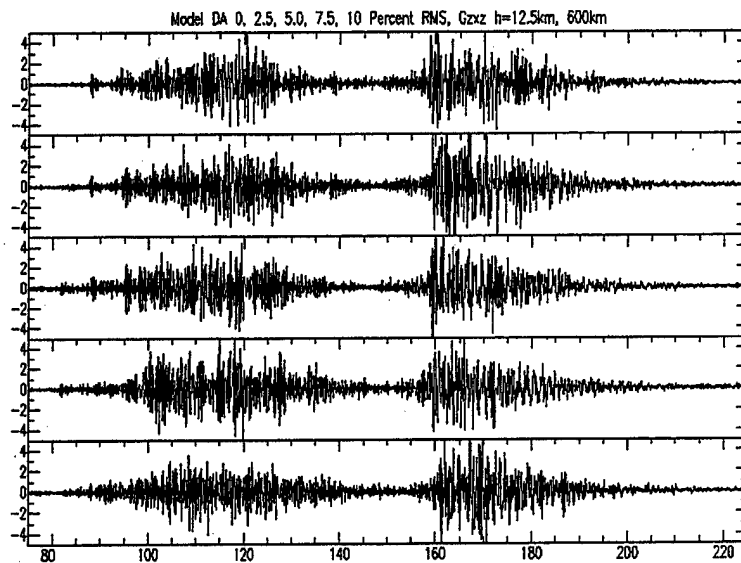


Figure 9. Vertical seismogram at 600 km from an earthquake source ($h=12.5\text{km}$) for layered model DA with 0%, 2.5%, 5.0%, 7.5%, and 10% velocity variation.

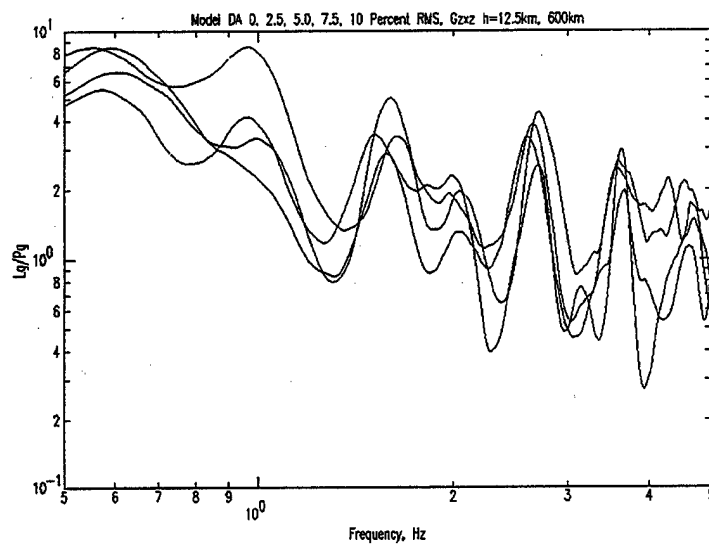


Figure 10. Vertical component Lg/Pg ratio at 600 km from an earthquake source ($h=12.5\text{km}$) for layered model DA with 0%, 2.5%, 5.0%, 7.5%, and 10% velocity variation.

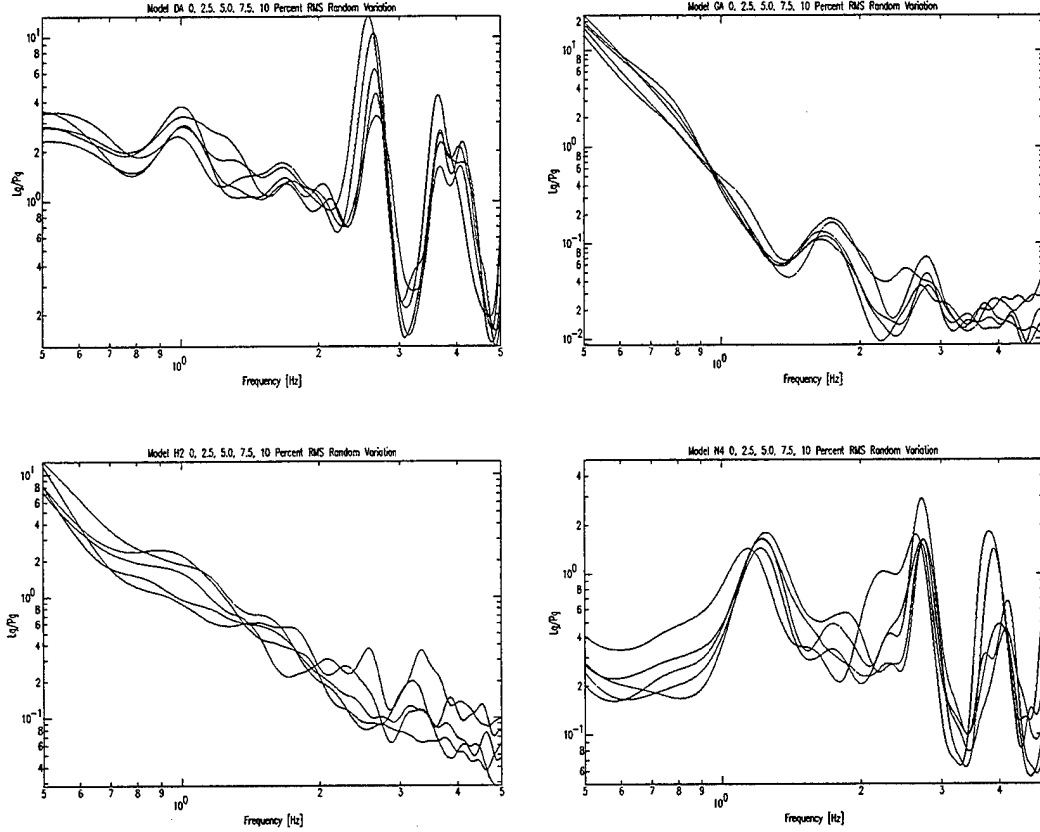


Figure 11. Vertical component Lg/Pg spectral ratios for models DA, GA, H2, and N4 for an explosion source ($h=1\text{km}$) and 0, 2.5, 5, 7.5, and 10% RMS random velocity layers. Note that the general character of the Lg/Pg ratio while very different for each background model, is not altered much by the introduction of random velocity layers.

2.3 Frequency Dependent Attenuation, $Q(f) = Q_0 * f^\eta$

We have examined three simple crustal attenuation models, Q1, Q2, and Q3 in detail.

$$Q1) Q_\mu(f,z) = Q_{0\mu} * f^\eta, \eta = 0, Q_{0\mu} = \beta(z)/10 \text{ for } z > 0 \text{ m},$$

$$Q2) Q_\mu(f,z) = Q_{0\mu} * f^\eta, \eta = 0, Q_{0\mu} = \beta(z)/5 \text{ for } z > 3 \text{ km, low } Q \text{ surface layers}$$

$$Q3) Q_\mu(f,z) = Q_{0\mu} * f^\eta, \eta = 0.5, Q_{0\mu} = \beta(z)/5 \text{ for } z > 3 \text{ km, low } Q \text{ surface layers.}$$

The choice of model Q3 was based on three requirements.

- Low Q surface layers are required to attenuate unwanted short-period low-group velocity higher modes and Rg that propagate in the low-velocity near surface layers. We chose $Q_{0\mu} = 25$ for $0 < z < 1 \text{ km}$, $Q_{0\mu} = 75$ for $1 \text{ km} < z < 2 \text{ km}$ and $Q_{0\mu} = 150$ for $2 \text{ km} < z < 3 \text{ km}$.
- Average shear and compressional Q values in the crust must generally produce Lg/Pg ratios greater than unity near 1 Hz for earthquake mechanisms. We found

that $Q_{0\mu} = \beta(z)/5$ for $z > 3$ km would yield reasonable Lg/Pg ratios near 1 Hz, while the model $Q_{0\mu} = \beta(z)/10$ attenuated Lg too much.

- Short-period earthquake Lg/Pg spectral ratios as a function of frequency should generally remain above or near unity from 1 to 5 Hz. We chose Q proportional to $f^{0.5}$ in order to keep Lg/Pg ratios from declining too steeply as a function of increasing frequency.

Figures 12 and 13 show compilations of Lg/Pg spectral ratios from Bennett *et al.* (1997). Earthquake Lg/Pg ratios generally slowly decrease with increasing frequency.

Synthetics from a variety of crustal models suggested that in order to produce earthquake-like Lg/Pg ratios greater than unity near 1 Hz the higher Q_0 's of models Q2 and Q3 are preferred to those of model Q1. Also, to keep Lg/Pg ratios relatively flat as a function of frequency, an increase in Q as a function of frequency ($\eta > 0$) is needed. The Lg/Pg ratios above 1 Hz for models Q1 and Q2 were too small and do not agree with observations. Lg Q increasing with increasing frequency is commonly observed (Nuttli, 1981; Goncz *et al.*, 1986, Gupta and McLaughlin 1987; Campillo *et al.*, 1985; Mitchell 1981) with η between 0 and 1. It should be noted that numerous researchers have found a negative correlation between Q_0 and η ; the higher Q is at 1 Hz, the slower it increases with increasing frequency. Therefore, it may be possible to reproduce many of the observed results by assuming higher Q_0 's with somewhat smaller values of $\eta < 0.5$. Also, in tectonic regions with lower 1 Hz Q values, the value of η may be higher.

Figures 15-17 show explosion and earthquake Green's functions computed for the three Q models. The velocity model D2 is well suited to show off the differences between Q1, Q2, and Q3. The earthquake Lg amplitudes are too small in models Q1 and Q2 for both the broadband and the higher frequency seismogram (0.5 Hz highpass Figure 14 and 3.0 Hz highpass Figure 16). A shallow explosion excites very slow unrealistic waves in the near surface layers in model Q1 (Figure 15).

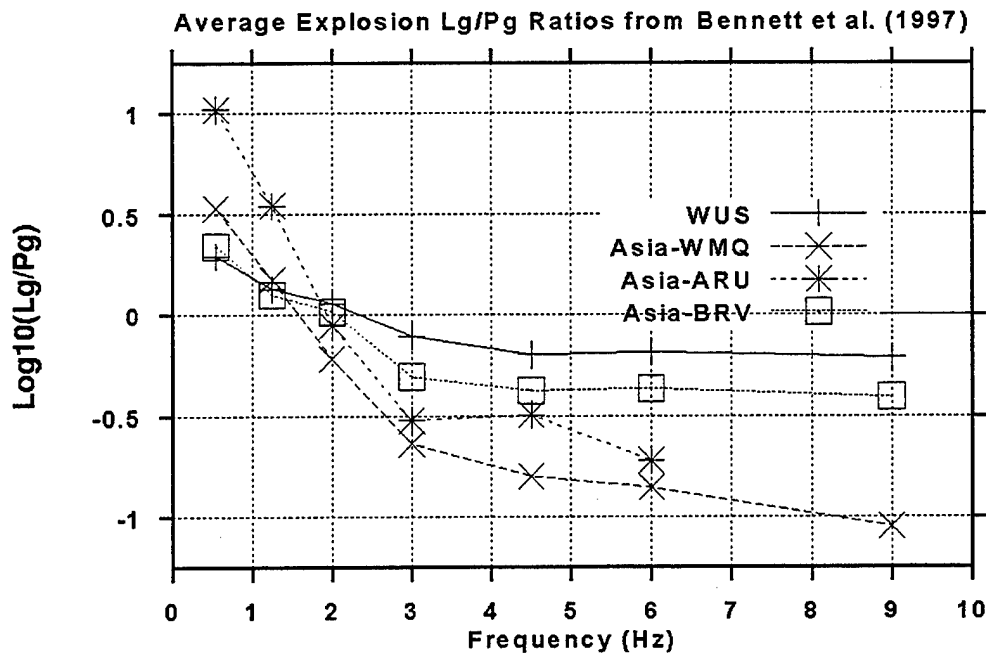


Figure 12. Compilation of average explosion Lg/Pg spectral ratios from Bennett *et al.* (1997) for explosions in Asia and Western US. Note that the average Lg/Pg is generally greater than unity for frequencies at and below 1 Hz.

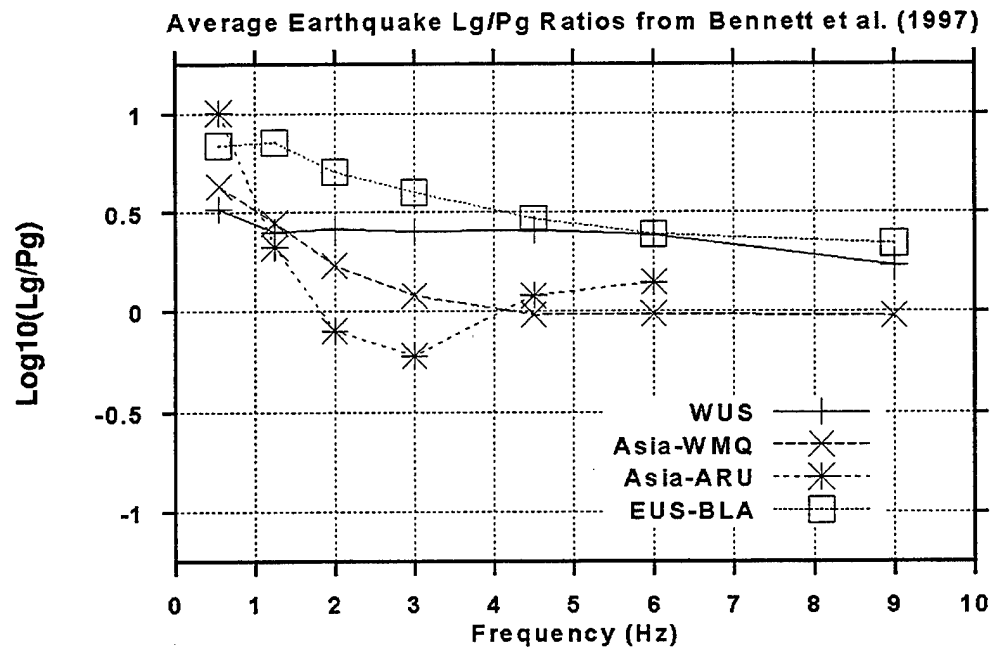


Figure 13. Compilation of average Lg/Pg spectral ratios from Bennett *et al.* (1997) for earthquakes in Asia, Western US, and Eastern US. Note that Lg/Pg is generally greater than unity for frequencies below 5 Hz with the exception of the ARU data. The average earthquake curves are generally above the corresponding explosion curves at frequencies above 1 Hz.

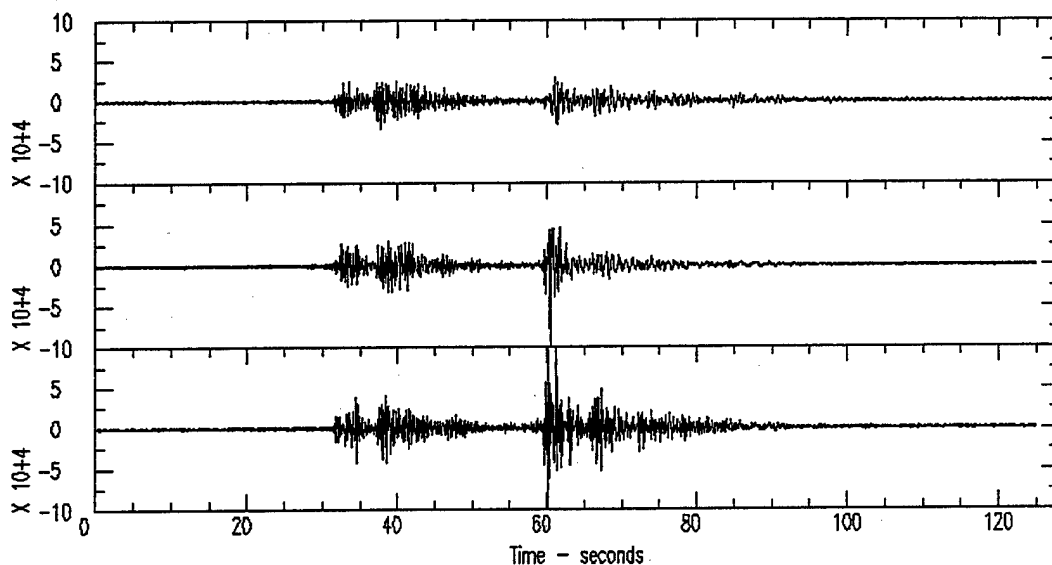


Figure 14. Comparison of vertical component synthetics (high pass at 0.5 Hz) at 200 km for three $Q(f,z)$ models and velocity model D2, Q1 (top), Q2 (middle), Q3 (bottom). A dip-slip double-couple source (Gzds) at 15 km depth is shown. The Lg amplitude is significantly increased relative to the Pg amplitude for $\eta=0.5$, $Q_0=\beta/5$, model Q3.

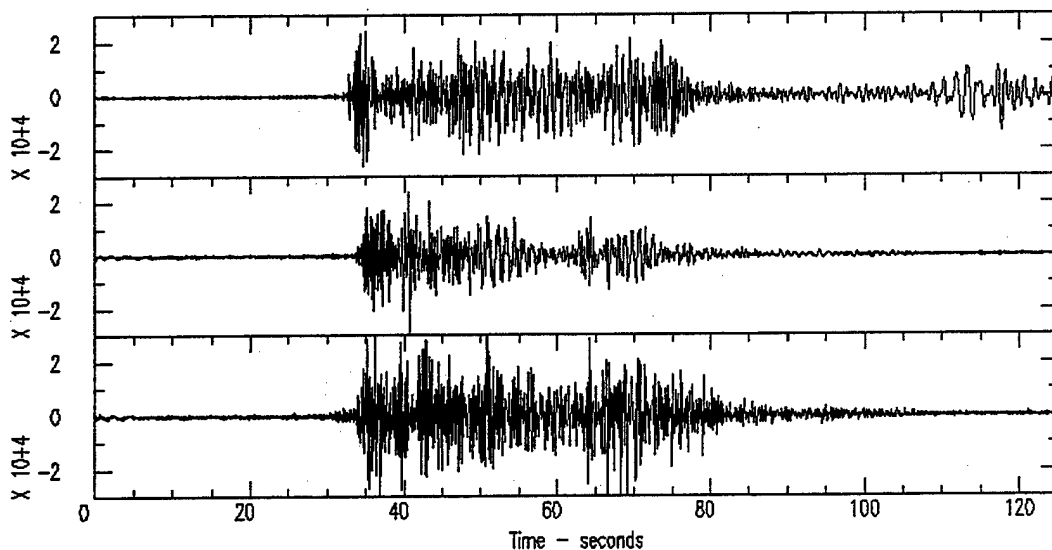


Figure 15. Comparison of vertical component synthetics (high pass at 0.5 Hz) at 200 km for three $Q(f,z)$ models and velocity model D2, Q1 (top), Q2 (middle), Q3 (bottom). An explosive source (Gzi) at 1 km depth is shown. The high Q surface layer model does not sufficiently attenuate the late arriving fundamental surface waves excited by the shallow explosive source. Also, it is clear that the Q1, high Q surface layer model contains too much shallow propagating energy in the Lg window that is absent in the low Q surface layer models, Q2 and Q3.

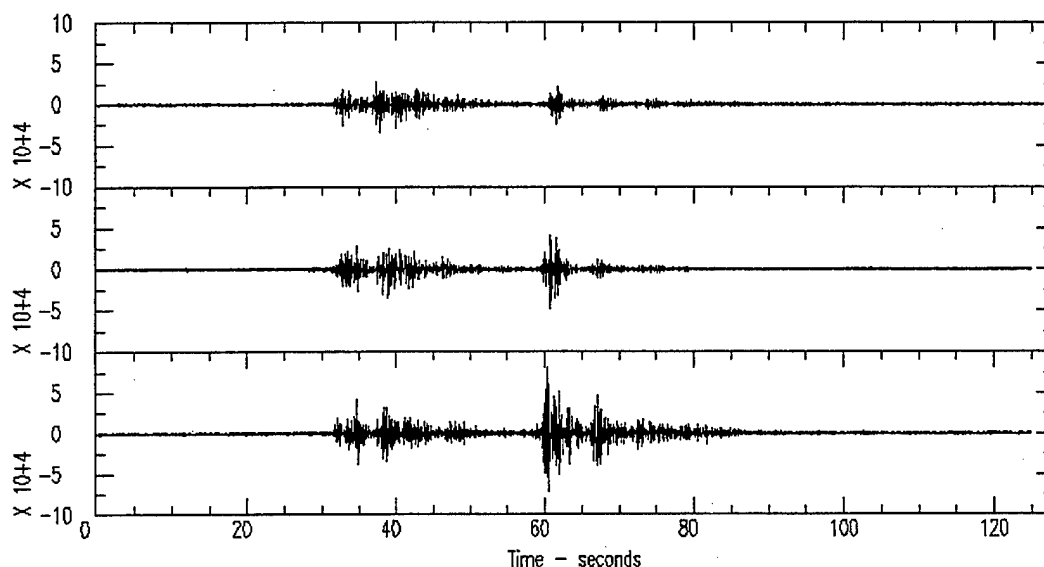


Figure 16. Comparison of vertical component synthetics (high pass at 3.0 Hz) at 200 km for three $Q(f,z)$ models and velocity model D2, Q1 (top), Q2 (middle), Q3 (bottom). A dip-slip double-couple source (Gzds) at 15 km depth is shown. The Lg amplitude is significantly increased relative to the Pg amplitude for $\eta=0.5$, $Q_0=\beta/5$, model Q3

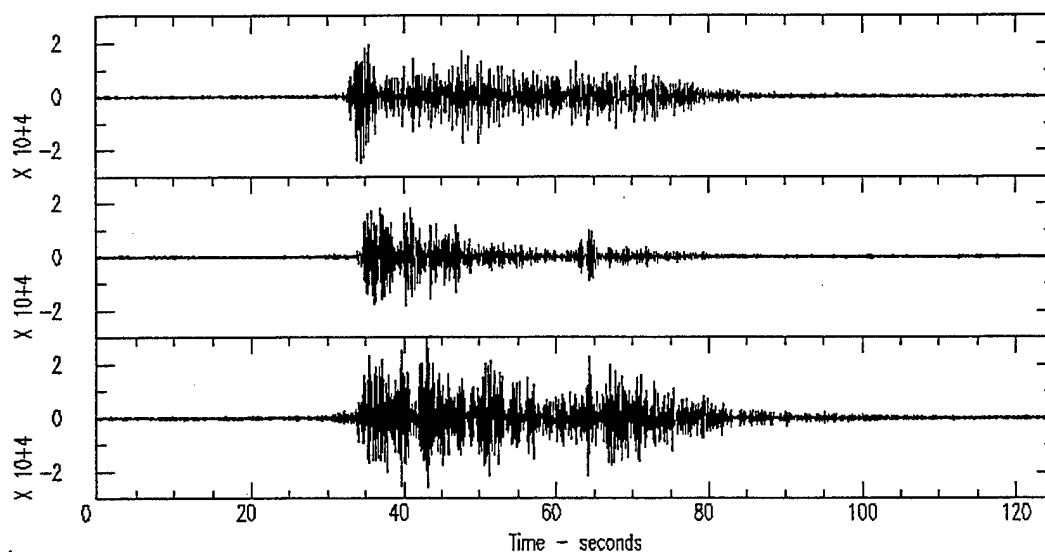


Figure 17. Comparison of vertical component synthetics (high pass at 3.0 Hz) at 200 km for three $Q(f,z)$ models and velocity model D2, Q1 (top), Q2 (middle), Q3 (bottom). An explosive source (Gzi) at 1 km depth is shown below. The Lg is almost non-existent in model Q2.

2.4 Acknowledgments

We wish to thank Al Geist and Bob Manchek of ORNL and UT for an excellent PVM tutorial at Supercomputing '95. Steve Day of SDSU provided many useful suggestions in the implementation of the wavenumber integration code.

2.5 References

- Anderson, J., W. E. Farrel, K. Garcia, J. Given, H. Swanger (1990a), "Center for Seismic Studies Version 3 Database: Schema Reference Manual," Technical Report C90-01, September 1990, Center for Seismic Studies, Arlington VA.
- Anderson, J., W. Farrel, K. Garcia, J. Given, and H. Swanger (1990b), "Center for Seismic Studies Database: Version 3.0 Structure," SAIC Report June 1990, SAIC, San Diego CA.
- Apsel R. J., and J. E. Luco (1983), "On the Green's Functions for a Layered Half-Space, Part II," *Bull. Seism. Soc. Am.*, 73, 931-951.
- Campillo, M., J. Plantet, M. Bouchon (1985), "Frequency Dependent Attenuation in the Crust Beneath Central France from Lg Waves: Data Analysis and Numerical Modeling," *Bull. Seism. Soc. Am.*, 75, 1395-1411.
- Christensen and Mooney, (1995), "Seismic Velocity Structure and Composition of the Continental Crust: a Global View," *JGR*, 9761-9788.
- Geist, A., A. Beguelin, J. Dongarra, W. Jiang, R. Manchek, V. Sunderam (1994), *PVM: Parallel Virtual Machine - A User's Guide and Tutorial for Networked Parallel Computing*, MIT Press, Cambridge, MA 279 pp.
- Gupta, I. N., and K. L. McLaughlin (1987a), "Attenuation of Ground Motion in the Eastern United States," *Bull. Seism. Soc. Am.*, 77, 366-383.
- Harvey, D. J. (1992), "A Systematic Study of the Effects of Crust and Upper Mantle Structure on Regional Seismograms," PL-TR-92-2138, ADA260231.
- McLaughlin, K. L., and B. Shkoller (1996), "Wavenumber Integration Synthetic Seismogram Calculations Using A Parallel Virtual Machine," Scientific Report No. 1, July 1996, submitted to Phillips Laboratory PL-TR-96-2284, ADA323186.
- Mitchell, B. J. (1981), "Regional Variations and Frequency Dependence of Q_β in the Crust of the North America," *Bull. Seism. Soc. Am.*, 71, 1531-1538.
- Mooney, W.D, M.G. Laske, and T. G. Masters, (1996), "CRUST 5.0: A Global Crustal Model at 5 Degree X 5 Degree," *JGR* (submitted).
- Nuttli, O. W. (1981), "Similarities and Differences Between Western and Eastern United States Earthquakes, and Their Consequences for Earthquake Engineering," in *Earthquakes and Earthquake Engineering: the Eastern United States*, J. E. Beavers, Editor, Ann Arbor Science Publishers, Ann Arbor, Michigan, 25-51.
- SAC2000 Reference Manual, June 1995, LLNL, Livermore, CA, <http://www-ep.es.llnl.gov/tvp/sac.html>.
- Smith, D. D. (1978), *Numerical Solution of Partial Differential Equations: Finite Difference Methods* 2nd ed., Oxford University Press, 304 pp.

3.0 Finite Difference 3D Regional Scattering Calculations

3.1 Introduction

Numerical methods for 3D elastic wave propagation have made significant advances in the last decade due in part to better software, but largely due to exponential growth of computer capabilities. For a fixed price, computer memory and speed roughly double every 18 months (popularly known as "Moore's Law"). Provided such technological advances continue it will be another decade or more before 3D computations are as economical as 1D computations today. 3D computations require 8 times more memory and 16 times more CPU time than comparable 1D computations. For example, computation by wavenumber integration of a record section of 0.5 Hz regional Green's functions from 0 to 200 km at 0.5 km intervals requires about 1/20th the time as a section of 3D waveforms for a single source (hours versus days). While the suite of 3D seismograms is far richer than the 1D record section, the bandwidth and range of the 3D computation is far more limited than the 1D computation. With this in mind, it is beneficial to leverage 1D numerical methods as much as possible in understanding 3D results and devising hybrid methods for seismogram calculation.

Seismologists have developed extensive insight into the nature of wave propagation in layered earth models using 1D methods. Layered earth model synthetics correctly predict many of the gross features of regional seismograms. Distinct regional phases such as Pn, Pg, Sn, Lg, and Rg propagate as loosely coherent wave packets with well defined group velocities for large distances in crustal and upper mantle waveguides. 3D methods aim to predict how these phases are affected by scattering. For some cases we can view the 3D scattering as a perturbation upon the waveguides. From the point of view of modal summation methods, we can examine how the "modes" defined by the average 1D layered structure exchange energy with increasing range. Alternatively, we can view the outgoing wavefield from the point of view of wavenumber integration or phase screen methods. We can view the scattering as converting energy from one wavenumber into energy at a different wavenumber.

In this section, we report on work we have done to analyze the scattered wavefield computed using 3D elastic finite differences with modal summation and wavenumber spectra on phase screens. We compute scattered waves in 3D velocity models constructed by adding random perturbations to a mean crustal model. The total elastic wavefield (3 components of particle velocity) is saved on vertical planes at selected distances from the source. We then estimate the modal spectra and the wavenumber spectra on those planes. We compare these spectra with computations for a layered structure in order to gain insight into the scattering process.

Tres3D with recursive grid refinement was used to compute complete 3D elastic wave propagation in a 3D laterally heterogeneous model. Tres3D is a 2nd order explicit finite difference code for 3D rectangular meshes. It requires a minimum of 10 cells/wavelength and the grids were designed to provide a bandwidth from 0 to 0.6 Hz. Sources are inserted as moment tensors. Recursive grid refinement (RGR) described in McLaughlin and Day (1995) uses nested grids to decrease memory and CPU time. Fine zoning is used

in the crust (250 m), coarser zoning is used in the upper most mantle (500 m) and the coarsest zoning (1000 m) is used in the deepest mantle. Moderate to high attenuation is used in the mantle to suppress reflections from the bottom of the grid and the coarser grids. The sources were placed at $X = 0$, $Y = 0$ at depths of $Z = -0.5$ km and $Z = -12.5$ km. A reflection symmetry axis was used as a boundary condition on the $Y = 0$ and $X = 0$ planes to reduce the size of the problem by a factor of 4. The geometry is diagrammed in Figure 3.1-1.

The computation was performed over a 200 by 100 by 100 km volume and run to durations of about 100 seconds. The recursive grid refinement was used with 21 grids and a total of 10 million cells. Each computation required about 3 CPU days on a DEC 2100 5/250 workstation to complete the 7.3×10^{11} cell-cycles.

A list of computations is given in Table 1. Two source types were modeled: an explosion source with $M_{xx} = M_{yy} = M_{zz}$ centered at a depth of 0.5 km and a "double-couple" source with $M_{xx} = -M_{zz}$, $M_{yy} = 0$ at a depth of 12.5 km. Lateral heterogeneity was limited to the crust and upper most mantle. The mantle was a homogeneous half-space and a simple linear gradient was chosen for the background crustal structure. The background velocity model is shown in Figure 18. In order to introduce lateral heterogeneity we used the following procedure:

- 1) Generate a 3D random array, $r(x,y,z)$, uniformly distributed between -1 and 1, sampled at $x = 0, \dots, x_{\max}$, $y = 0, \dots, y_{\max}$, $z = z_{\min}, \dots, 0$ to fill the volume $x_{\max} = 128$ km, $y_{\max} = 32$ km, $z_{\min} = -32$ km, with sampling intervals $dx = 1.0$ km, $dy = 1.0$ km, and $dz = 0.5$ km.
- 2) Smooth the random numbers in the X and Y directions with a 3-point smoothing operator (1,1,1). Re-scale the array to an RMS value of 1.
- 3) For a given (x,y,z) location in the crust ($z > z_{\min}$) set the S-velocity to $\beta^{-1}(x,y,z) = \beta^{-1}_0(z) (1 + \text{RMS} * r(x,y,z))$. For $x > x_{\max}$, or $y > y_{\max}$, or $z > z_{\min}$, the velocity is set to the background model. Run #1 was formulated with fluctuations specified in velocity instead of slowness.

This procedure introduces an-isotropic heterogeneity with characteristic lengths of about 1 km in the Z and X directions and 2 km in the Y direction. Figures 20 and 21 show two ways to visualize this lateral heterogeneity.

Snap shots of vertical particle velocity from Run#1 (5% RMS velocity variation, explosion source) along the $Y = 0$ plane are shown in Figures 22 through 27. Complexity of the wave propagation is immediately evident. Development of the refracted P and Pn can be seen at $T = 15$ seconds as well as development of the moho reflection, PmP. Lg can be best seen at later times $T = 20, 25$, and 30 seconds as an interference of up-going and down-going waves in the crust. The short-period fundamental Rayleigh wave, Rg, can be seen running along the surface at about 2.5 km/s. The disorganized wavefield behind the Rg wavefront is simply labeled "coda". Waveforms from Run#1 are shown in Figure 28 to illustrate that Rg is the most significant arrival at these distances on the surface, and it is systematically delayed and attenuated by the random fluctuations.

Table 1. Computational Runs.

Run #	Source Type	RMS Variation	Source Depth (km)
Run 1	$M_{xx} = M_{yy} = M_{zz}$	5% velocity	0.25
Run 2	$M_{xx} = M_{yy} = M_{zz}$	5% slowness	0.25
Run 3	$M_{xx} = M_{yy} = M_{zz}$	5% slowness	0.25
Run 4	$M_{xx} = M_{yy} = M_{zz}$	0	0.25
Run 5	$M_{xx} = M_{yy} = M_{zz}$	5% slowness	0.25
Run 6	$M_{xx} = M_{yy} = M_{zz}$	7.5% slowness	0.25
Run 7	$M_{xx} = -M_{zz}, M_{yy} = 0$	7.5% slowness	12.5
Run 8	$M_{xx} = -M_{zz}, M_{yy} = 0$	0	12.5

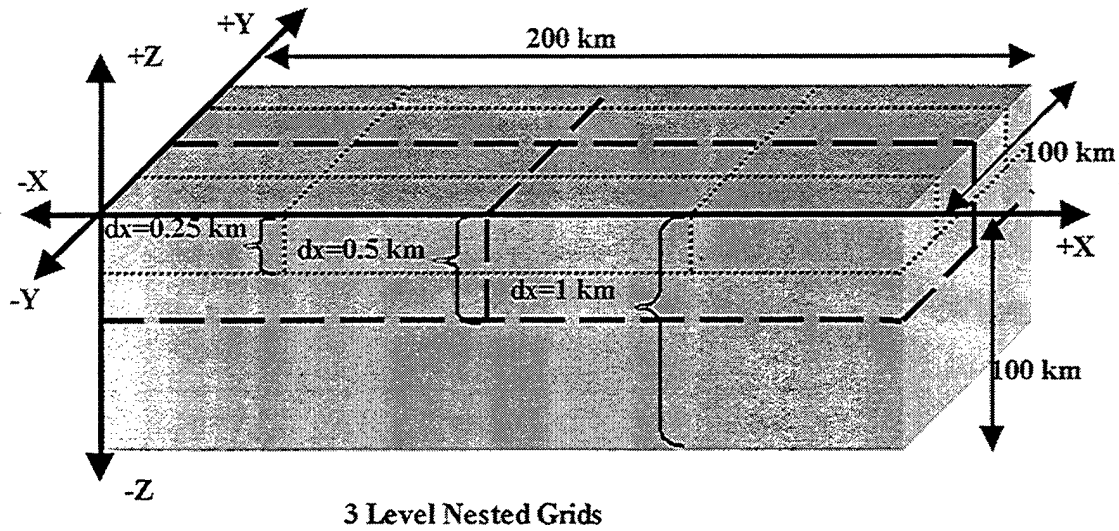


Figure 18. Diagram of 3 levels of nested grids; 1 grid on level 1, 4 grids on level 2, and 16 grids on level 3 for a total of 21 grids. Each grid contains $64 \times 64 \times 128 = 524,288$ cells for a total of 11 million cells. The root grid ($102.4 \times 102.4 \times 204.8$ km) has 1 km cells. The 4 intermediate level grids fill the space to a depth of 51.2 km with 0.5 km cells. The 16 finest level of grids fill the space to a depth of 25.6 km with 0.25 km cells. A reflection symmetry axis was placed on the $Y = 0$ and $X = 0$ planes. The $Z = 0$ plane is a free surface.

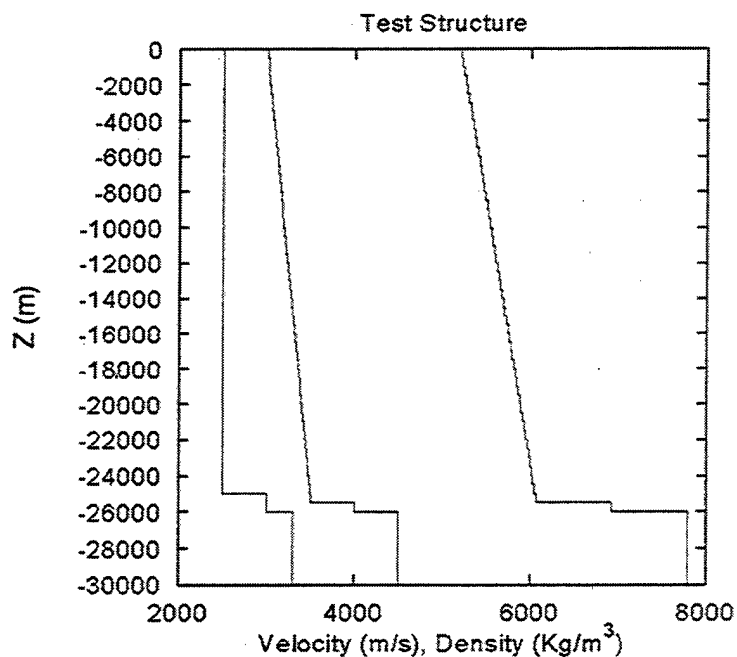


Figure 19. Plot of the test structure used in all computations. P- and S-wave velocities in the crust are simple gradients with Poisson's ratio of 0.25. The Moho consists of two steps at 25 and 26 km..

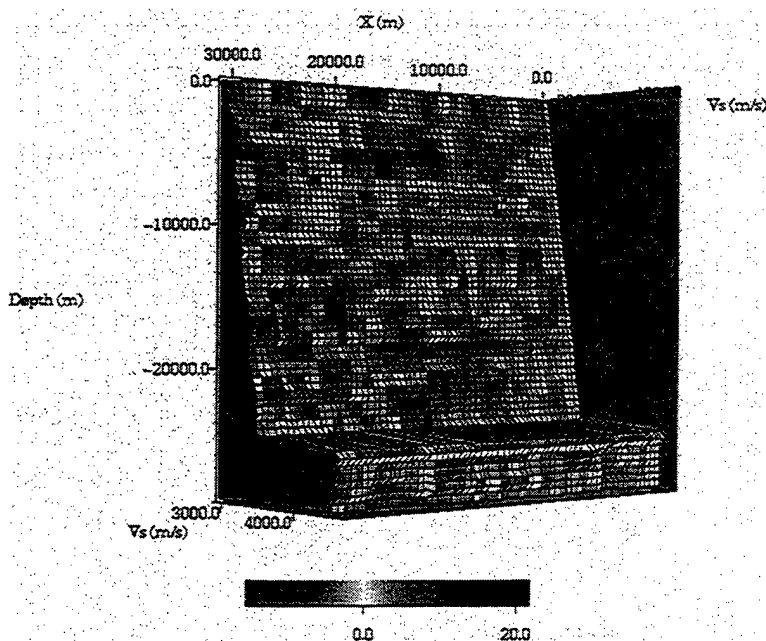


Figure 20. Shear velocity along a $Y = \text{Constant}$ slice of the model. The horizontal anisotropic variation is clearly evident.

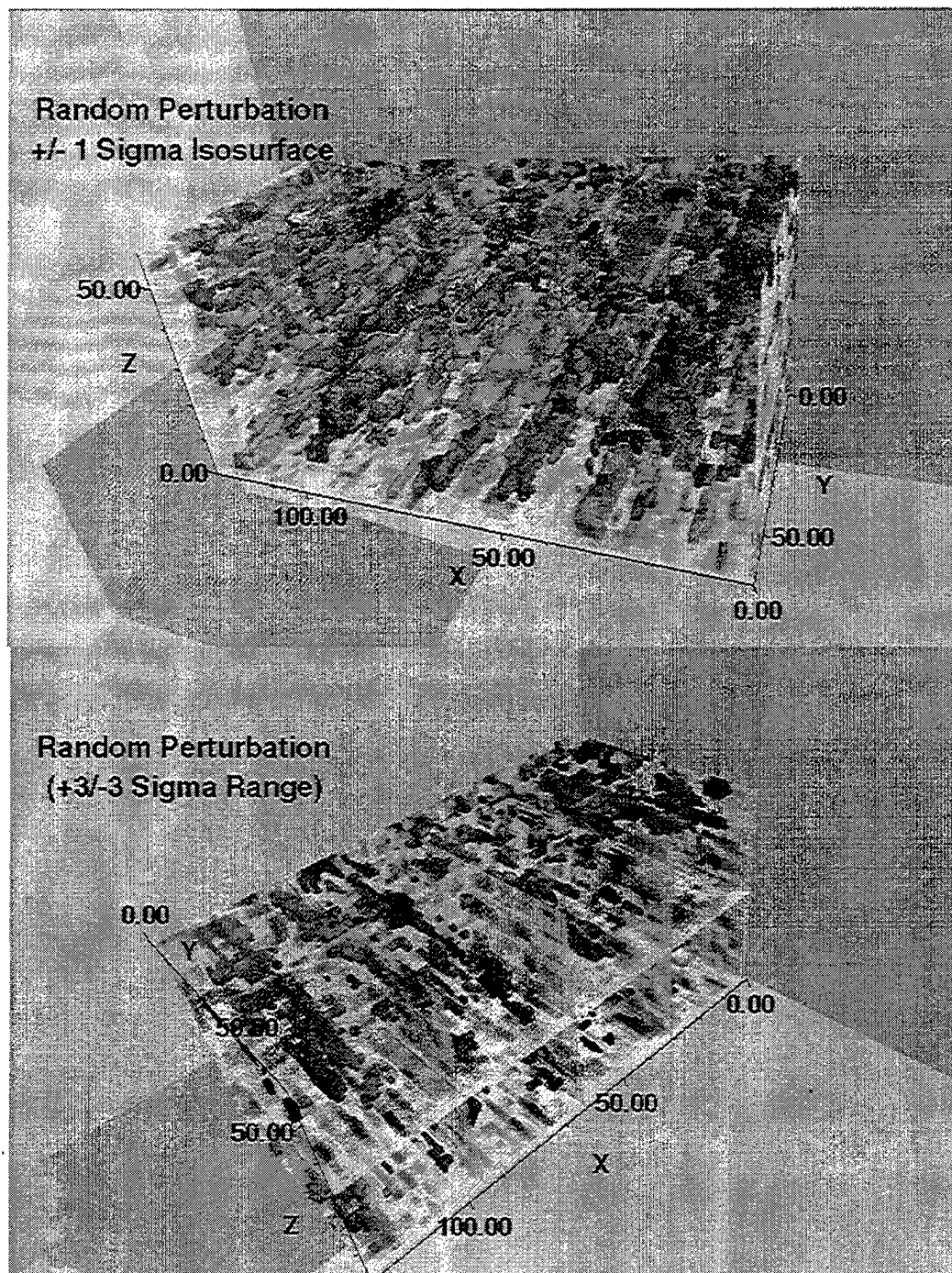


Figure 21. Visualization of the 3D random variation. Isosurfaces with absolute variation greater $\pm 1\sigma$ are shaded in the top image. Regions within $\pm 1\sigma$ are transparent. The lower image shows the same with $\pm 3\sigma$. These images help visualize the cores of the scatterers. Note the elongation of the scatterer cores in the Y direction.

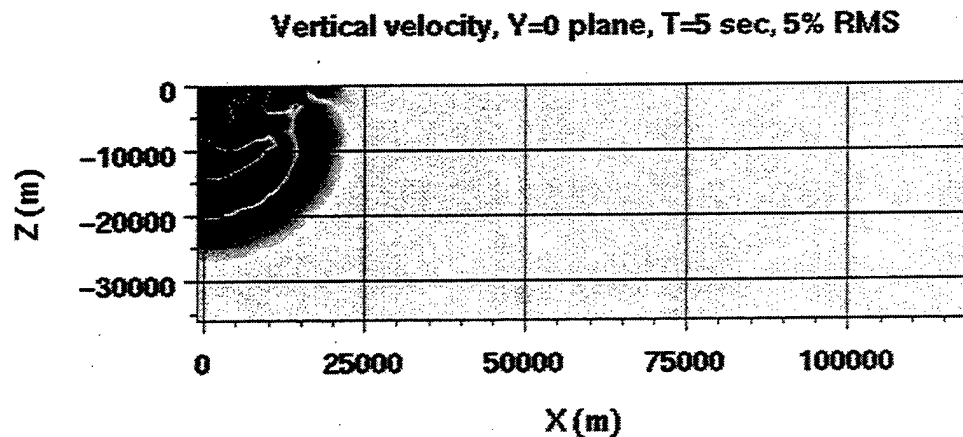


Figure 22. Run #1 snap shots of vertical particle velocity on the $Y = 0$ plane, at $T = 5$ seconds.

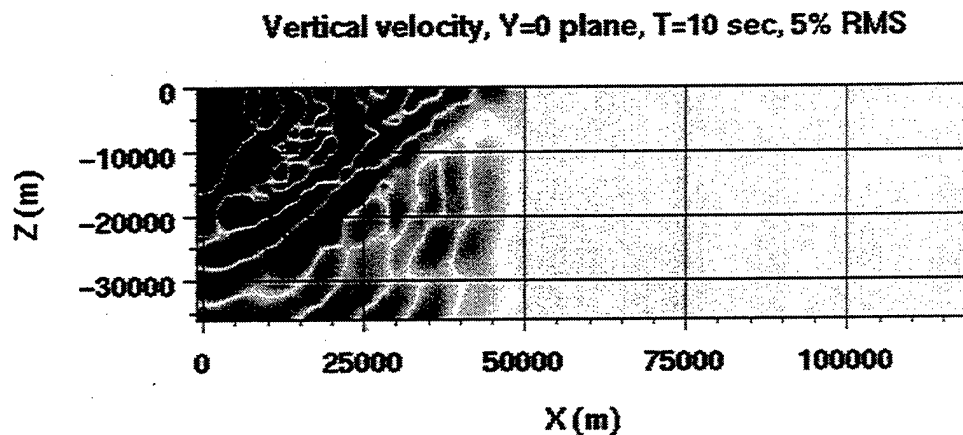


Figure 23. Run #1 snap shots of vertical particle velocity on the $Y = 0$ plane, at $T = 10$ seconds.

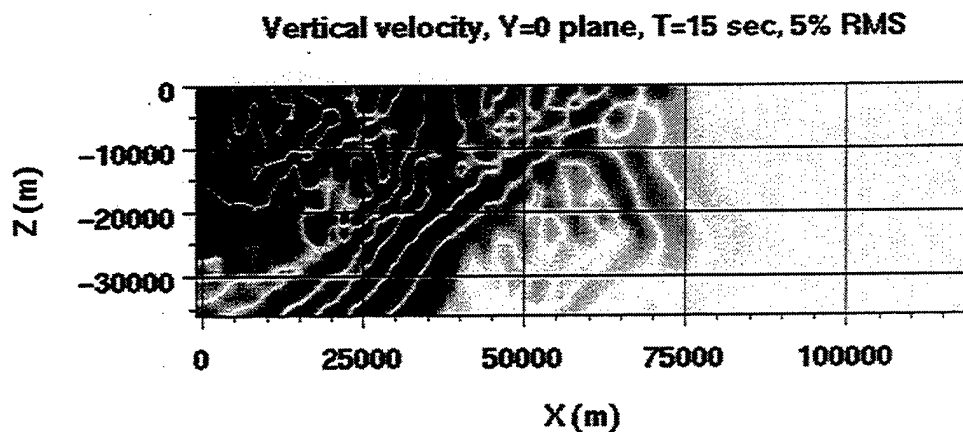


Figure 24. Run #1 snap shots of vertical particle velocity on the $Y = 0$ plane, at $T = 15$ seconds.

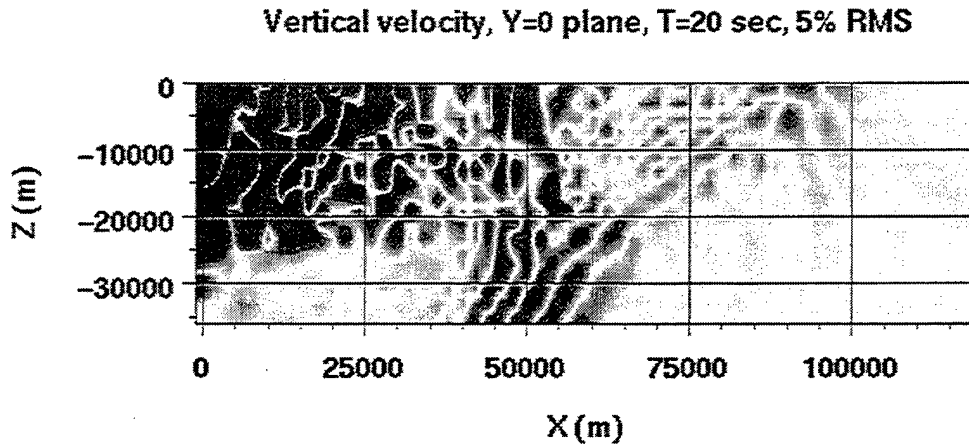


Figure 25. Run #1 snap shots of vertical particle velocity on the $Y = 0$ plane, at $T = 20$ seconds.

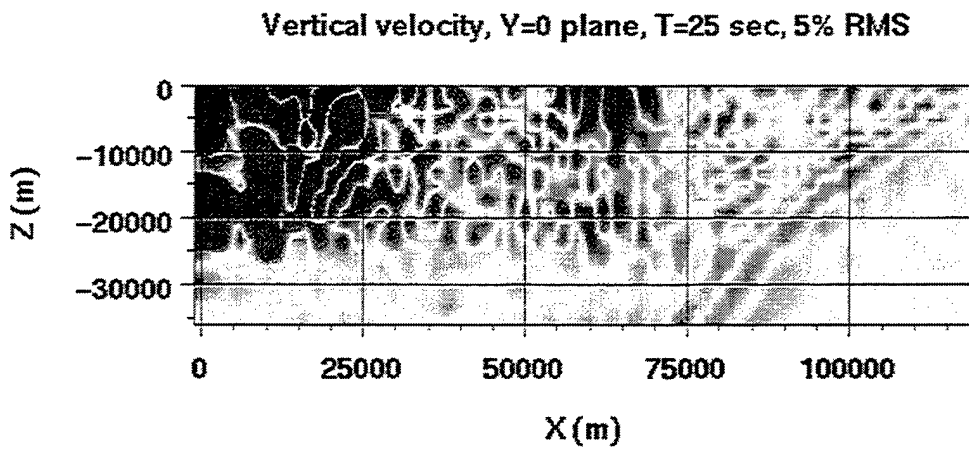


Figure 26. Run #1 snap shots of vertical particle velocity on the $Y = 0$ plane, at $T = 25$ seconds.

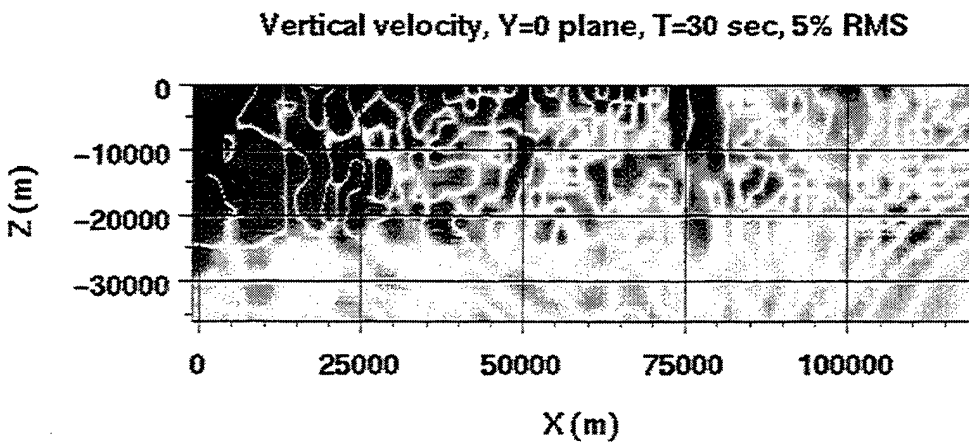


Figure 27. Run #1 snap shots of vertical particle velocity on the $Y = 0$ plane, at $T = 30$ seconds.

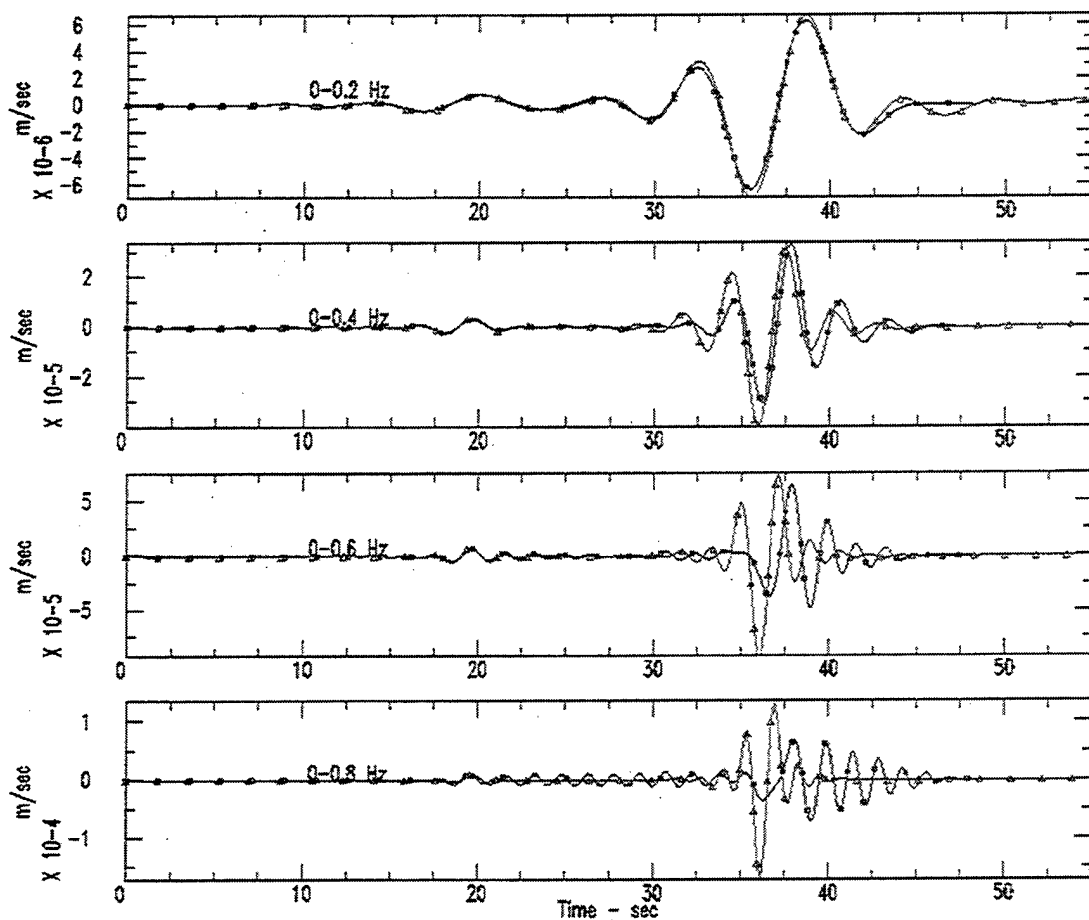


Figure 28. Comparison of finite difference and wavenumber integration synthetics for Run #1 (5% RMS, explosion source) at 100 km for lowpass filters 0.2, 0.4, 0.6, and 0.8 Hz (top to bottom). Note that the Rg is unaffected in the lowest bandwidth and is increasingly attenuated and delayed with increasing frequency. Frequencies above 0.6 Hz are affected by grid dispersion.

3.2 Modal Spectra

Modal summation is a common approach to either analyze or compute wave propagation in a layered structure (Aki and Richards, 1980). The methods for seismogram synthesis have a long and fruitful history. In particular, Lg can be analyzed as groups of the P-SV and/or SH modes. Several researchers have described weak scattering as mode-mode conversion, where energy is transferred from one mode to another. We wish to take advantage of the machinery developed for modal summation and estimate a "modal spectra" or a "modal decomposition". We write the vertical seismogram at frequency, f , depth, z , and distance, Δ , as a mode sum, $S_z(f, z, \Delta) = \sum_{j=1, N} C_{zj}(f, \Delta) E_{zj}(z, f)$, where $E_{zj}(z, f)$ is the j 'th mode vertical eigenfunction at frequency, f (see Figures 29 and 30). Likewise for the radial seismogram, $S_r(f, z, \Delta) = \sum_{j=1, \dots, N} C_{rj}(f, \Delta) E_{rj}(z, f)$. We can then examine the modal spectra, $C_j(f, \Delta)$, as a function of frequency and distance. In order to estimate this modal spectra, we save the vertical and radial velocities at some distance for each depth

in the finite difference grid. Since the eigenfunctions are orthogonal, we should only need to compute an inner product between $S(f,z,\Delta)$ and $E_j(z,f)$ to compute the coefficients, $C_j(f,\Delta)$. However, the finite difference seismograms are only sampled at specific depths from the surface to a maximum depth and they contain wave types that are not present in the pure P-SV modes, such as Pn and Pg as well as scattered body waves. In short, the modes are not exactly orthogonal under the numerical quadrature and leakage can occur of the non modal waves into the modes. It helps to use both the vertical and radial motion to constrain the modal estimates. We use a stripping procedure described below.

- 1) start with mode $j = 1$ and set

$$S'_Z(f,z,\Delta) = S_Z(f,z,\Delta)$$

$$S'_R(f,z,\Delta) = S_R(f,z,\Delta)$$

- 2) estimate the normalized inner product over depth from z_1 to z_{nz}

$$E_{Zj0}(f) = \sum_{k=1,nz} E_{Zj}(z_k,f)^2$$

$$E_{Rj0}(f) = \sum_{k=1,nz} E_{Rj}(z_k,f)^2$$

$$C_j(f,\Delta) = (1/2) \sum_{k=1,nz} (S'_Z(f,z_k,\Delta) E_{Zj}(z_k,f) / E_{Zj0}(f) + S'_R(f,z_k,\Delta) E_{Rj}(z_k,f) / E_{Rj0}(f)) dz_k$$

- 3) strip the j 'th component from the observed seismogram

$$S'_Z(f,z,\Delta) = S_Z(f,z,\Delta) - C_j(f,\Delta) E_{Zj}(z,f)$$

$$S'_R(f,z,\Delta) = S_R(f,z,\Delta) - C_j(f,\Delta) E_{Rj}(z,f)$$

- 4) if $j < N$ then increment the mode number j to $j + 1$ and go to step 2.

We find this stripping procedure is relatively insensitive to whether we start with mode $j = 1$ and increment to mode $j = N$, or start with mode $j = N$ and decrement to mode $j = 1$. Amplitude of the residual seismogram is small in comparison to the original seismogram. Generally, about 90% of the seismogram energy is accounted for by the modal spectra. Obviously, this simple quadrature rule could be refined, but we believe that the modal spectra estimated in this way provide insight into the scattering processes. Figure 31 shows modal spectra, $C_j(f,\Delta)$, for Run#2 (5% RMS) and Run#4 (0% RMS) at a range of 120 km. Note the modal cut-off where the number of modes increase with increasing frequency. Mode 1 corresponds to the fundamental Rayleigh wave. Modes 2 through 8 are the higher modes that exist in the test structure for frequencies up to 0.6 Hz. The modes are normalized to unit vertical amplitude at the free surface. Therefore, the spectral amplitudes can be interpreted in terms of the amplitudes of the modes of an observed surface vertical seismogram. The modes, however, may not necessarily arrive at their customary group velocities nor as isolated modes in the time domain. Clearly, the fundamental is the largest amplitude mode from 0.1 to about 0.4 Hz for both the laterally homogeneous and heterogeneous models. The fundamental is the largest mode for the laterally homogeneous model (Run#4) at all frequencies, but has been reduced to an amplitude comparable to the higher modes at frequencies greater than about 0.4 Hz in the laterally heterogeneous model (Run#2). We interpret this as scattering from the fundamental into higher modes by lateral heterogeneity. A simple way to illustrate this is shown in Figure 32 where we form a ratio between the modal spectra from Run#2 and Run#4. This modal spectral ratio demonstrates the enhancement of energy in the higher

modes at nearly all frequencies at the expense of the fundamental. Likewise, we show a ratio of modal spectra at 60 km to spectra at 120 km in Figure 33.

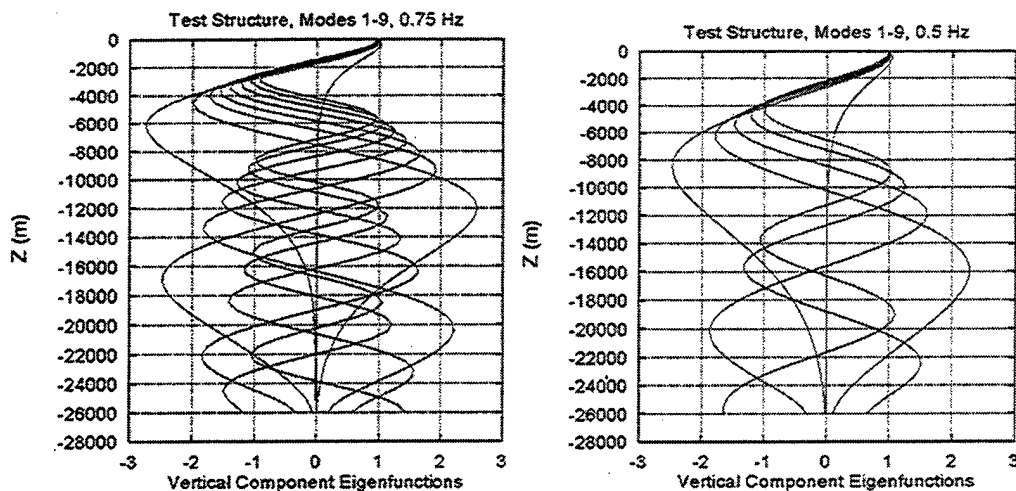


Figure 29. Plots of P-SV modes at 0.5 Hz (right) and 0.75 Hz (left) for the test structure shown in Figure 19. Note that the fundamental mode has very little motion below 4 km (at 0.75 Hz) and below 5 km (at 0.5 Hz). The higher modes sample the entire crust.

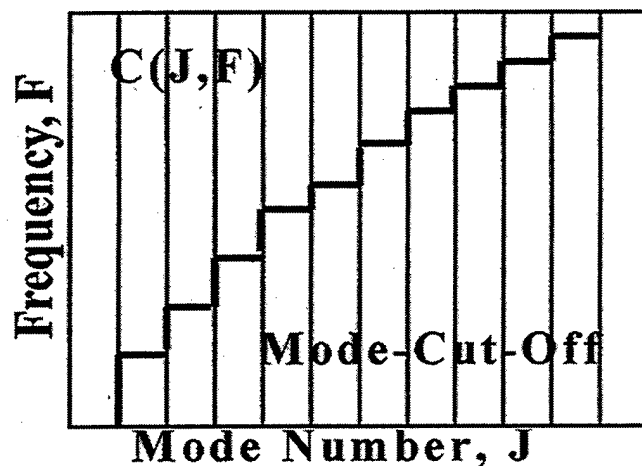
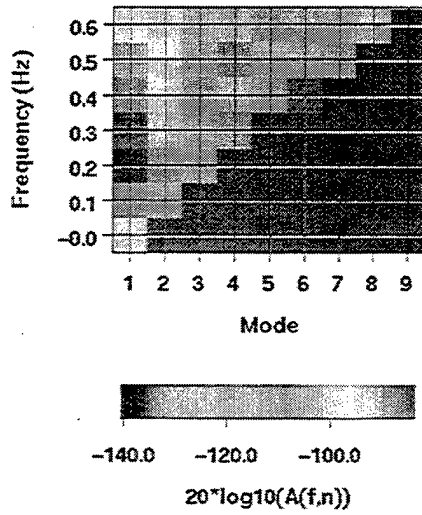
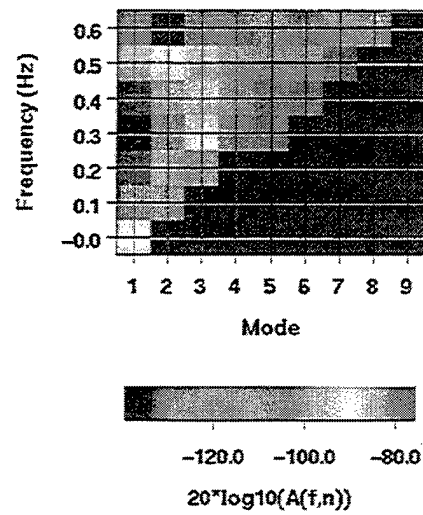


Figure 30. Diagram of Modal Spectra. $C(J,F)$. $C(J,F) = 0$ to the right of the modal cut-off line.

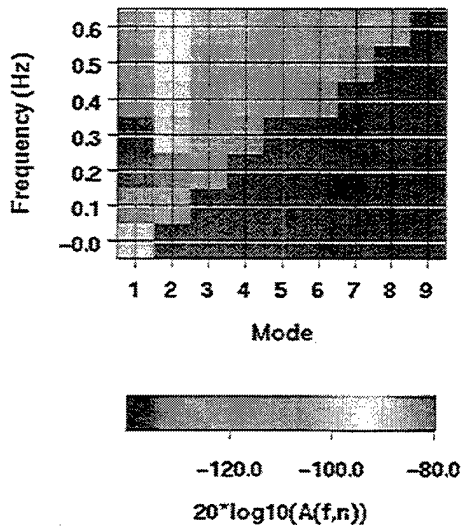
Modal Spectra, 120 km Vertical Component, 0% RMS



Modal Spectra, 120 km Vertical Component, 5% RMS



Modal Spectra, 60 km Vertical Component, 0% RMS



Modal Spectra, 60 km Vertical Component, 5% RMS

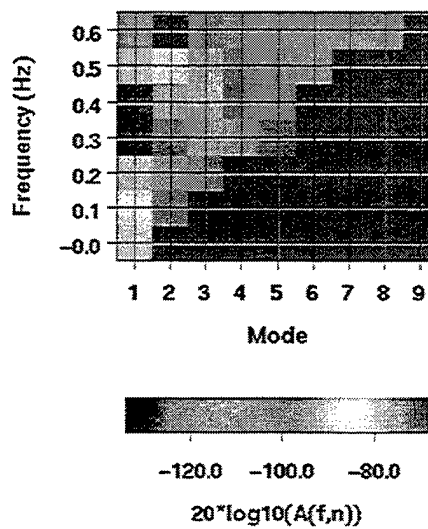


Figure 31. Modal spectra at 120 km (top) and 60 km (bottom) for models with 0% RMS (left) and 5% RMS (right) lateral heterogeneity.

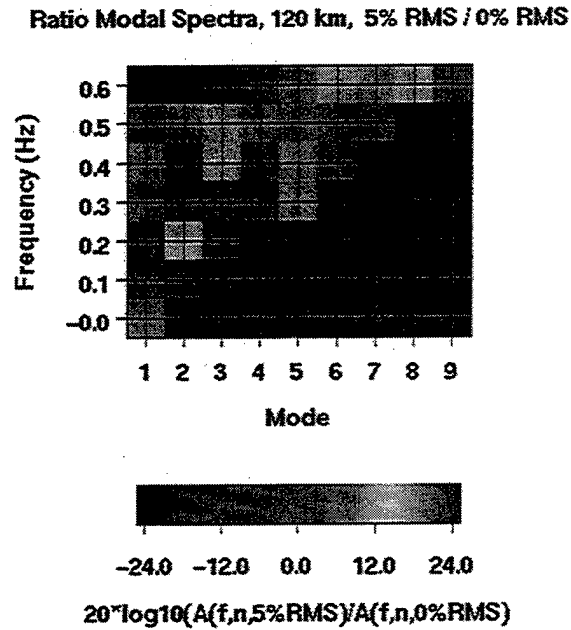


Figure 32. Modal Spectral Ratio at 120 km 5% RMS model / 0% RMS model. Yellow and Red shades are modes enhanced w.r.t. the background model. Blue and purple shades are modes deficient w.r.t. the background model.

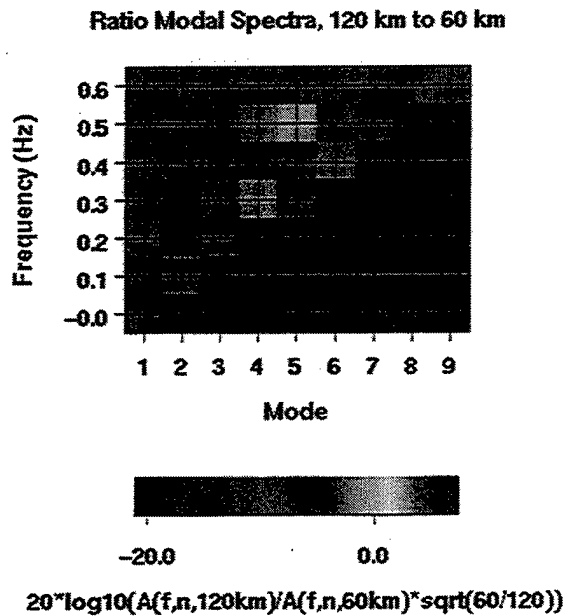


Figure 33. Ratio of 120 km to 60 km. This spectral ratio highlights modes that have lost or gained energy between 60 and 120 km.

3.3 Wavenumber Spectra

While the modal spectra are useful descriptions of the crustal wavefield, they do not provide a complete description. In order to obtain this more complete description of the wavefield, we have taken a cue from other numerical methods for computing wavefields such as wavenumber integration or phase screen methods. We save the 3 components of motion on a 32 km by 32 km vertical plane perpendicular to the nominal direction of propagation ($X = \text{constant}$) and compute a 3D FFT of the seismograms to transform them from the (y, z, t) domain to the wavenumber-frequency (F_y, F_z, f) domain. $F_z = f s_z$, and $F_y = f s_y$ are the wavenumbers for propagation in the vertical (Z) and transverse (Y) directions respectively; s_z and s_y are the slowness components in the vertical and transverse directions respectively.

$$S(F_y, F_z, f) = \sum e^{-iF_y y_i} \sum e^{-iF_z z_k} \sum e^{-i\omega t_j} s(y_i, z_k, t_j)$$

The diagram in Figure 34 can be of help in understanding these wavenumber-wavenumber spectra. Note that because the finite difference calculations are performed with a symmetry axis at $Y = 0$, the phase plane spectra are also symmetric about the Z axis, $S(F_y, F_z) = S(-F_y, F_z)$. Waves traveling straight at the phase plane are plotted at the origin of the diagram. Upgoing waves arriving perpendicular to the plane plot along the positive F_z axis, while downgoing waves arriving perpendicular to the phase plane plot along the negative F_z axis. Off azimuth waves (side-swipe) plot away from the F_z axis. Since there is a minimum velocity in the crustal waveguide, all propagating waves must plot inside a circle given by $(F_z^2 + F_y^2)^{1/2} = f / \beta_{\min}$. Waves with $F_z = f s_z < f / \beta_{\text{mantle}}$ are trapped in the crust where β_{mantle} is the shear wave velocity of the mantle below the moho. Because the phase plane has finite dimensions, there are side lobes. Also, all outgoing waves are not planar and they have curvature as they impinge upon the phase plane; even in the absence of lateral heterogeneity, the spectra are not confined strictly to the F_z axis. Therefore, for each wavenumber spectra for a laterally heterogeneous model we show the corresponding wavenumber spectra for the strictly layered structure for comparison. And, in order to gain insight into the side lobes and impulse response to a curved wavefront at a selected distance, we plot the impulse response of some cylindrical waves incident upon the 32 km by 32 km phase plane at 120 km from a point source in Figures 35 and 36.

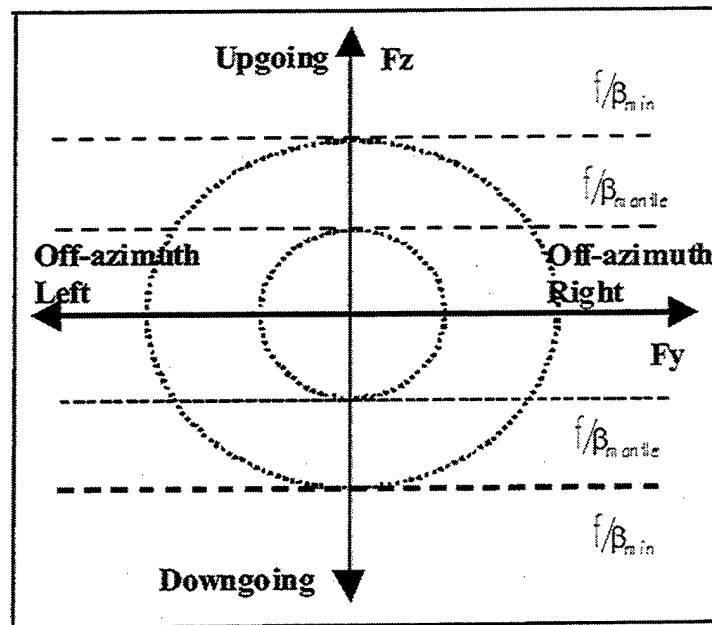


Figure 34. Diagram of wavenumber-wavenumber spectra at frequency, f . All wavenumber spectra in this paper are symmetric about the vertical wavenumber axis because of a reflection symmetry on the $Y = 0$ plane in the finite difference calculations.

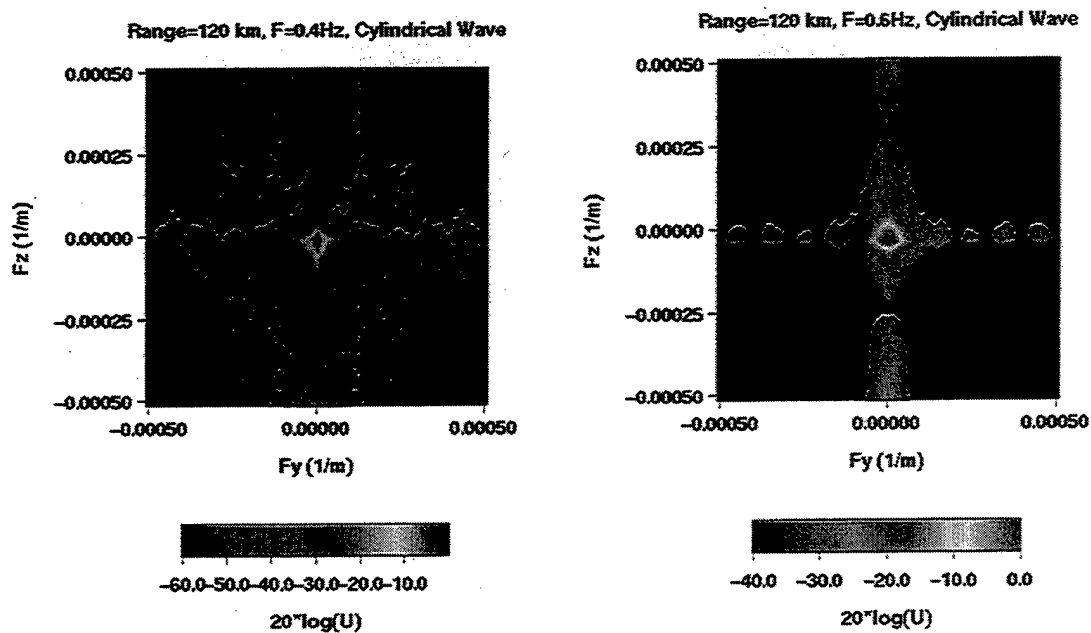


Figure 35. Phase plane wavenumber impulse response for a cylindrical wave, 120 km from the source at 0.4 (left) and 0.6 Hz (right).

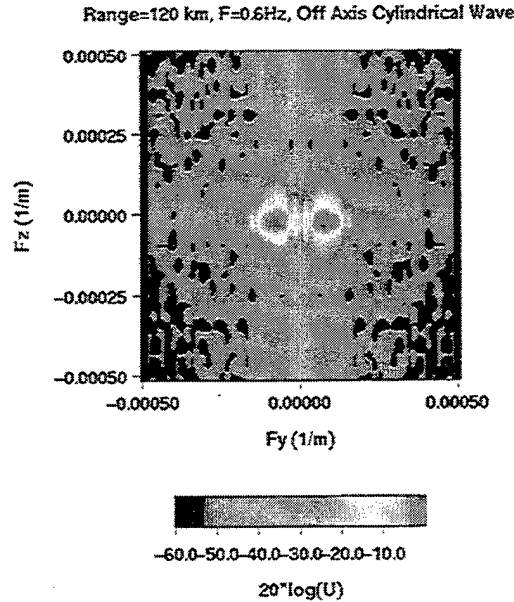


Figure 36. Phase plane wavenumber impulse response for an off-axis cylindrical wave, 120 km from the source at 0.6 Hz.

Wavenumber-wavenumber spectra at 120 km and 0.6 Hz from Run # 2 (5% RMS explosive source) and Run #4 (0% RMS, explosive source) are compared in Figures 37-39. In the absence of scattering, on-azimuth up-going and down-going waves with vertical slownesses near 0.3 sec/km (apparent vertical velocity about 3 km/sec) are particularly strong on the vertical and radial components of motion (Z and X). Presumably these correspond to the developing Lg wavetrain. Energy with vertical slownesses less than 0.2 sec/km is presumably related to the developing Pg wavetrain as well as steeply incident P and S waves that should escape into the mantle. For all three components of motion, we see that scattering has stretched out the spectra in the F_y direction indicative of the off-azimuth energy. Scattering has generally lowered the on-azimuth energy. Note that the transverse particle motion (Y component) is not identically zero for the laterally homogeneous case since the $X = 120$ km plane is only perpendicular to the direct waves at $Y = 0$. The scattered Y component wavenumber spectra become very complicated and fill a larger wavenumber region.

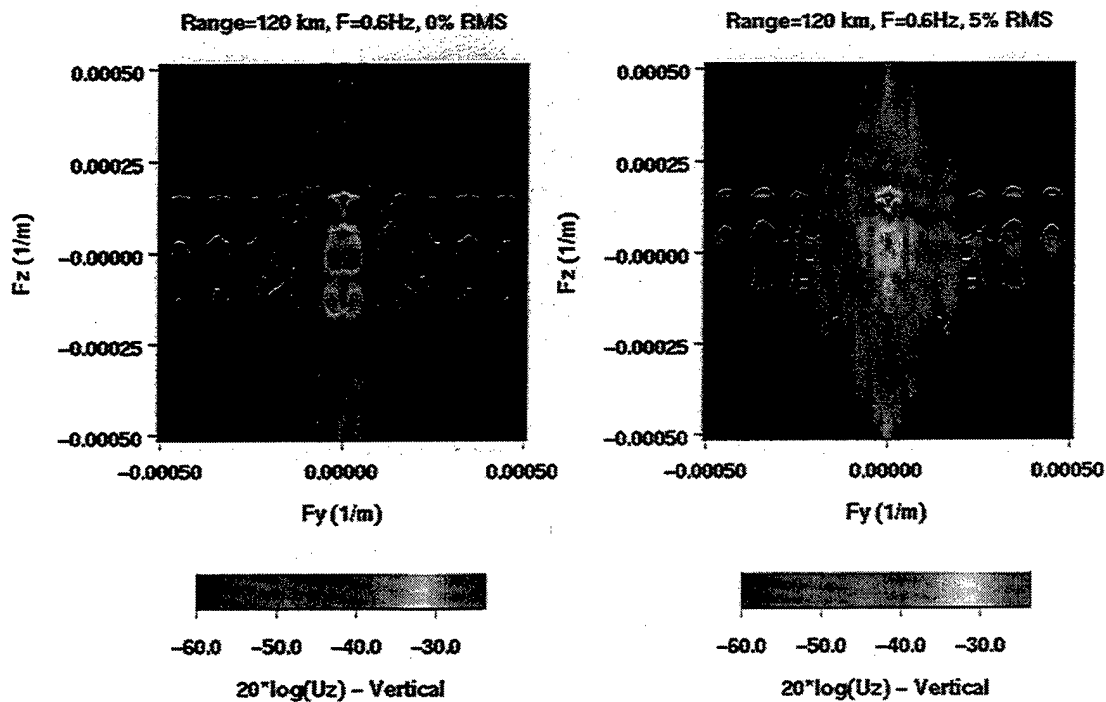


Figure 37. Wavenumber spectra of the vertical component velocity field on a $Y = 120$ km phase plane at 0.6 Hz for the 5% RMS (right) and 0% RMS (left).

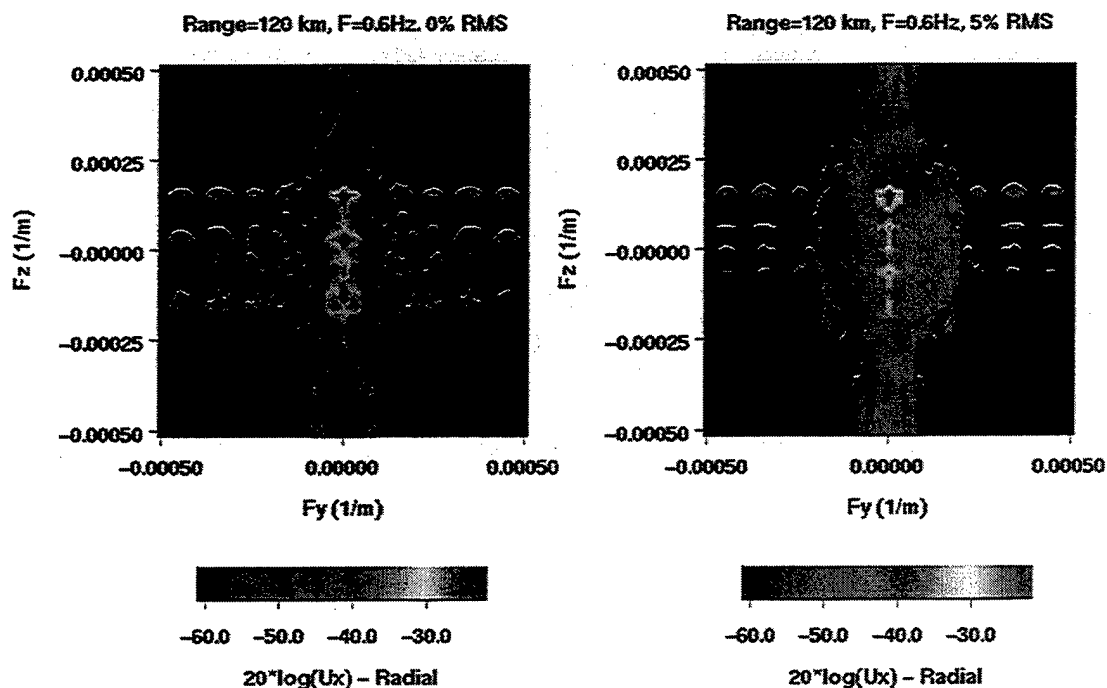


Figure 38. Wavenumber spectra of the radial component velocity field on a $Y = 120$ km phase plane at 0.6 Hz for the 5% RMS (right) and 0% RMS (left).

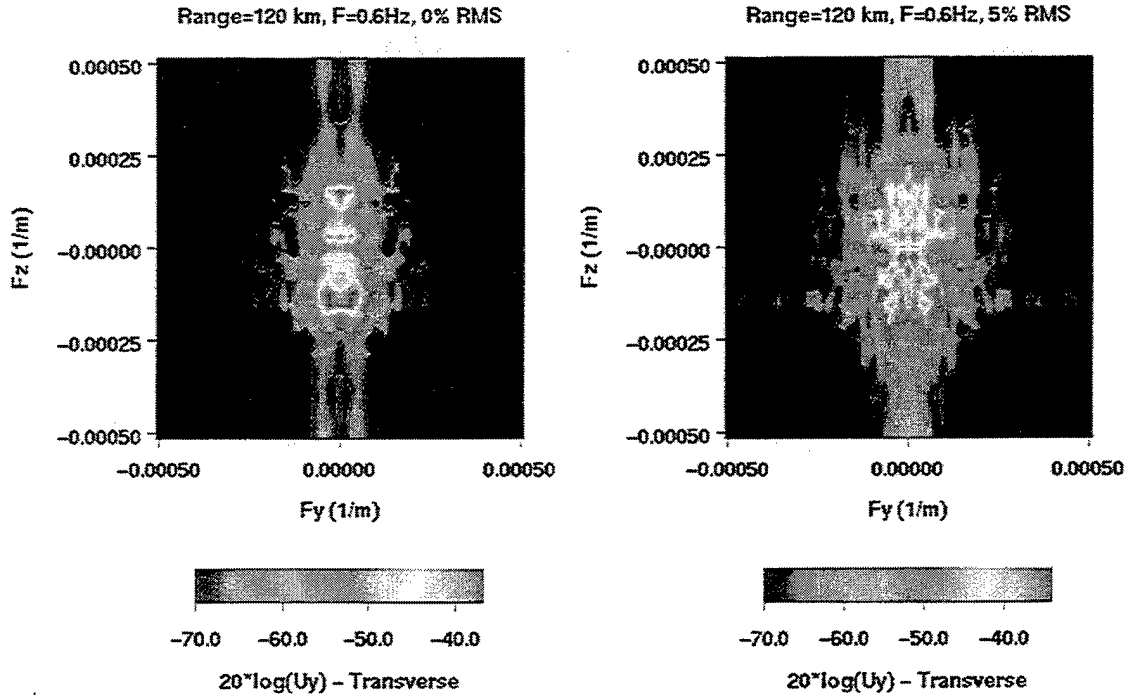


Figure 39. Wavenumber spectra of the transverse component velocity field on a $Y = 120$ km phase plane at 0.6 Hz for the 5% RMS (right) and 0% RMS (left).

3.4 Conclusions

Modal and wavenumber spectra of phase planes provide tools to analyze finite difference simulations of regional scattering. Modes serve as a convenient set of basis functions and have a straight forward interpretation. Modal spectral ratios can be used to estimate scattering attenuation of each mode and the general transfer between modes. Wavenumber spectra are perhaps more difficult to visualize but they provide means to visualize off-azimuth waves and waves that are not necessarily trapped in the crustal waveguide.

Fundamental mode dispersion looks significantly different for the randomized models than predicted by the average model. The scattering both attenuates the R_g and introduces significant group delay. If scattering makes a significant contribution to fundamental Rayleigh attenuation, seismologists should be careful interpreting the apparent group velocities and the inferred shallow velocities.

Conversion from the fundamental R_g becomes increasingly important with increasing frequency. With only moderate heterogeneity (5% RMS) the P-SV modes are rapidly approaching equilibrium at distances less than 100 km for frequencies above 0.5 Hz. Likewise, both off-azimuth P-SV and SH energy is significant at 60 km.

3.5 Acknowledgements

We would like to thank Ru-Shan Wu for stimulating discussions which led to the F-K analysis of phase planes.

3.6 References

- Aki, K. and P. Richards (1980), *Quantitative Seismology, Vol. 1*, Freeman and Company, 557 pp.
- Liu, Y. B. and Wu, R. S. (1994), "A Comparison Between Phase-Screen, Finite Difference and Eigenfunction Expansion Calculations for Scalar Waves in Inhomogeneous Media," *Bull. Seism. Soc. Am.*, 84, 1154-1168.
- Wu, R.-S. (1994), "Wide-Angle Elastic Wave One-Way Propagation in Heterogeneous Media and An Elastic wave Complex-Screen Method," *J. Geophys. Res.*, 99, 751-766.
- McLaughlin, K. L., and S. M. Day (1994), "3D Elastic Finite - Difference Seismic Wave Simulations," *Computers in Physics*, 8, No. 6, 656-666.

4.0 Permeable Hose Characteristics and Noise Reduction For Infrasound Monitoring

4.1 Summary

The proposed CTBT infrasound monitoring network consists of between 50 and 60 4-station microbarograph arrays. Many of the infrasound stations will be co-located or adjacent to seismic systems and work in concert. Each infrasound station is intended to consist of a broadband microbarograph equipped with several hundred meters of noise reduction hose. The permeable hose design replaces Daniels microphone pipes for the purposes of spatially averaging wind eddy generated pressure fluctuations. Useful detection thresholds for infrasound stations will be directly related to the effectiveness of the noise reduction hose arrays. We present an analysis of the differential equations that describe the acoustics of infrasound recording with a permeable hose as opposed to the discrete set of coupled equations that have traditionally been used to describe a Daniels pipe. It is shown that a hose may be characterized by a characteristic time constant, τ_0 , and a characteristic length, λ_0 . The time constant is related to permeability of the hose and the characteristic length is related to both flow resistance and permeability of the hose. Signal-to-noise improvement is directly proportional to the characteristic length of the hose. The low pass filter corner frequency of the system is determined by the characteristic time. Wavelengths of the pressure field shorter than characteristic length are averaged over the length of the hose. A finite difference code, **Maxhose**, is described that computes response of a simple linear permeable hose. The finite difference code is used to model both operational hose designs as well as calibration configurations. Simulations of a single hose to atmospheric pressure fluctuations are presented for a white noise and a fractal noise model. A simple experimental calibration is described to measure the characteristic times and lengths of permeable hoses. Calibration results are shown for commercially available soaker hose. Typical measured characteristic times are between 10 to 20 milliseconds, while characteristic lengths are between 50 and 200 meters. Of particular note are the effects of hose degradation during a typical San Diego winter as demonstrated by a reduction in characteristic length of the hose by a factor of 2. An operational system would have experienced a comparable degradation of signal-to-noise over time. Simple calibration systems can be designed to track such hose characteristics.

4.2 Introduction

The proposed IMS infrasound monitoring system will contain approximately 50 to 60 primary infrasonic arrays scattered around the globe. These arrays, composed of three or more sensors, will often be co-located or near an IMS seismic station. The arrays will be designed to provide arrival time and azimuth of arrival of low-frequency 0.01 to 10 Hz sound waves propagating in the atmosphere. While the primary mission of the infrasound network will be to detect nuclear explosions detonated in the atmosphere, these stations may also serve in an ancillary mission to help identify large chemical blasts recorded at seismic stations. The final design of sensors and operational procedures for detection, location, and identification of infrasonic events are as yet still in flux. Uncertainties still

exist in the areas of 1) excitation as a function of source type (explosion, quarry blast, meteor, volcanic explosion) and size 2) propagation attenuation as function of distance and frequency, and 3) optimum sensor design, and data processing.

Figures 40 and 41 show projected detection capabilities in Log10 (Yield in Kt) for atmospheric explosions by the proposed IMS infrasound network. These network simulations show the proposed network should be able to provide 90% assurance of detection at 2 or more infrasound stations at the 1 Kt level for most of the world. The 90% detection capability rises above 1 Kt in the South Pacific for 3 or more detections. In order to make projections such as Figure 41, we require models for 1) the excitation of infrasound as a function of frequency, yield, and height of burst, 2) the attenuation of infrasound as a function of frequency and distance, and 3) the noise and signal recording responses of the recording systems as a function of frequency. However, our understanding of all three of these important factors are far from complete. Critical to the ability of the proposed networks to monitor near the 1 Kt threshold are the permeable hose noise reduction systems. Detection thresholds are inversely proportional to the signal-to-noise improvements expected by the hose systems.

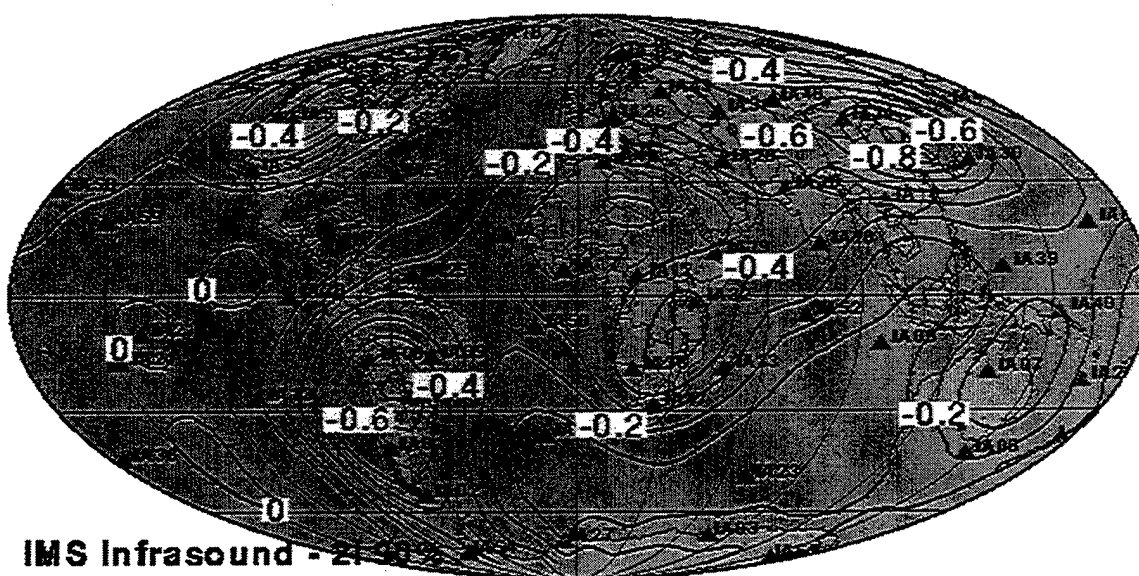


Figure 40. Contours of detection threshold in Log(Yield in Kt) at 90% probability for 2 infrasound detections at stations of the proposed IMS. Event scaling, attenuation relations, and noise levels based on Blandford and Clauter (1995) have been used. Thresholds are below 1 Kt nearly everywhere.

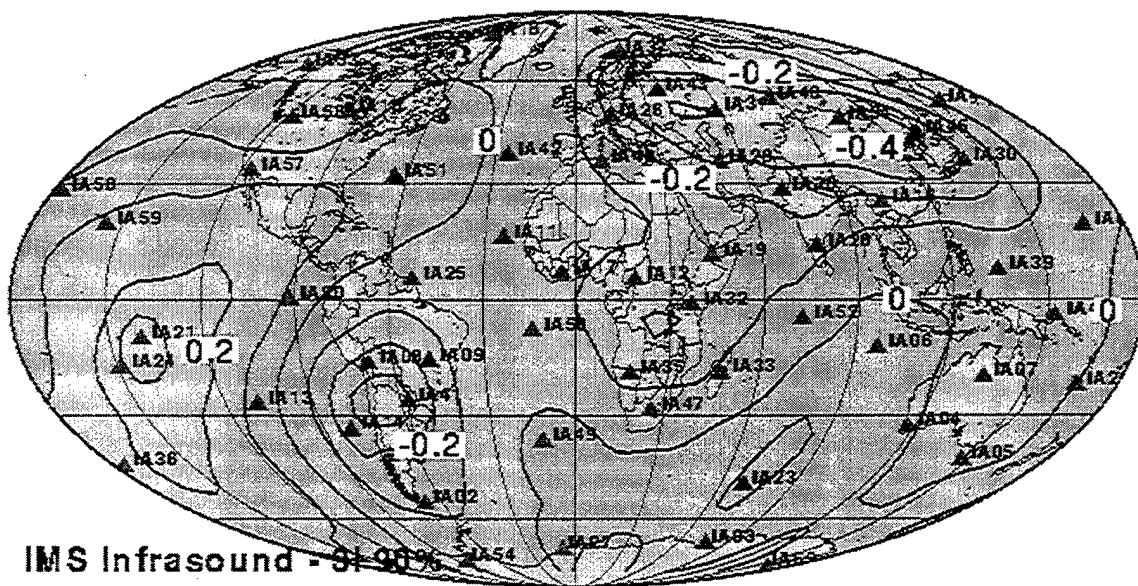


Figure 41. Contours of detection threshold in Log (Yield in Kt) at 90% probability for 3 infrasound detections at stations of the proposed IMS. Event scaling, attenuation relations, and noise levels based on Blandford and Clauter (1995) have been used. Thresholds reach 2 Kt in the South Pacific.

4.3 Theory of Noise Reduction Hoses and Their Calibration

The concept behind the use of a noise reduction hose relies on the fact that wind generated turbulent eddies have shorter apparent wavelengths than an infrasound signal arriving from great distance (Cook, 1971; Mack and Flinn, 1971; McDonald *et al.* 1971). The hose "averages" the local atmospheric pressure along its length and the incoherent eddies are "averaged" out.

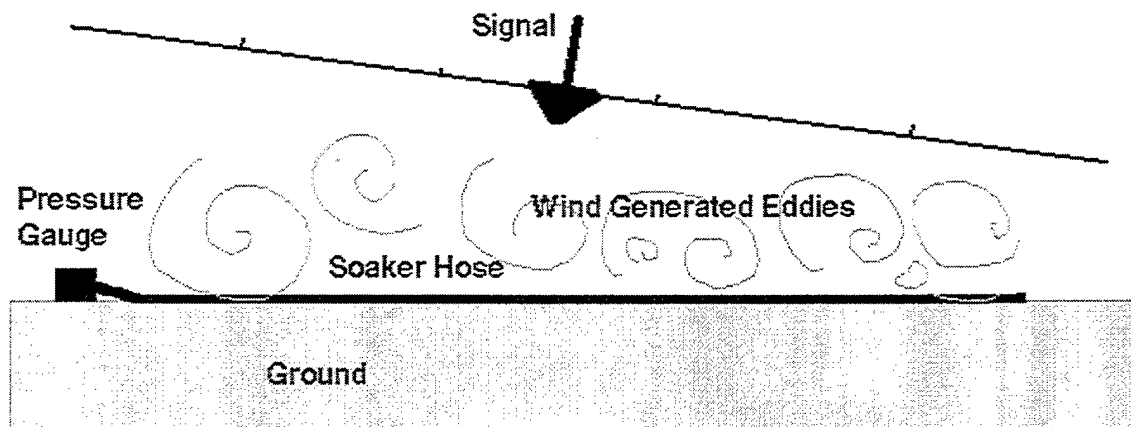


Figure 42. Wind generated eddies create pressure fluctuations and hence noise. The permeable hose acts to spatially "average" the pressure fluctuations.

The original Daniels pipe (Daniels 1959) was conceived as a discrete set of inlet ports along a length of pipe. Grover (1971) presents results for pipe arrays with hypodermic inlet ports, while Burrige (1971) presents a numerical solution to this discrete system of inlet ports, with a propagator method (a system of coupled equations). However, with the advent of soaker hose, the system is analogous to a transmission line or antennae problem and requires the solution of coupled partial differential equations.

An element of hose of length dx

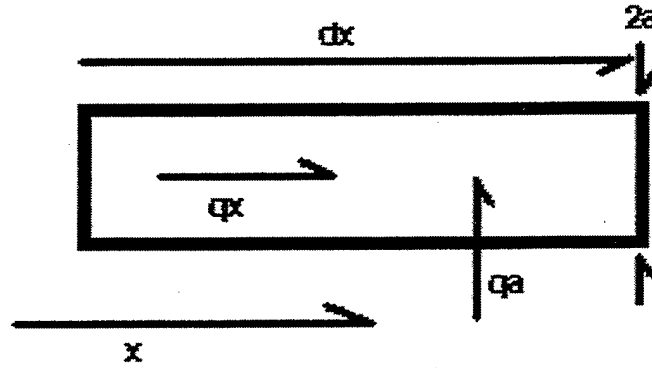


Figure 43. A hose element: length dx , radius a , flow in the x direction q_x , flow in/out q_a .

We consider an element of permeable hose of length dx and radius a . From conservation of mass we write,

$$\dot{m}(x, t) = \dot{\rho}(x, t) A dx = q(x, t) = q_o(x, t) - (q_x(x + dx, t) - q_x(x, t)),$$

where x is the distance along the hose, t is time, m is the mass of air in a length of hose dx , $\rho(x, t) = p(x, t)/(RT)$ is air density at temperature T , A is the cross sectional area of the hose, $q(x, t)$ is the total mass flow in the hose, $q_a(x, t)$ is the mass flow into the hose from outside per unit length, and $q_x(x, t)$ is the lateral mass flow along the hose in the positive x direction. We assume that air diffuses into and out of the hose proportional to the pressure difference, $(p_a(x, t) - p(x, t))$, where $p_a(x, t)$ is the pressure of the atmosphere outside the hose and $p(x, t)$ is the pressure inside the hose,

$$q_x = \rho A v = 2\pi a e (p_a(x, t) - p(x, t)) \partial x,$$

where e is a diffusion constant per unit length related to the permeability of the hose with radius, a . We next ignore inertial effects and assume that flow along the hose is steady state and proportional to the gradient of pressure along the hose,

$$q_x = \rho A v = (1/v) \partial p(x, t) \partial x,$$

where v is the hose flow resistance per unit length and v is the flow velocity. Grover (1971), gives excellent evidence that flow in noise reduction pipes can be described by simple Poiseuille flow where the hose resistance is proportional to viscosity, $v = 8\eta / \rho / \pi / a^4$, where η is the viscosity of air. We combine these equations to write a

partial differential equation for the pressure along the hose in terms of the external atmospheric pressure,

$$2\pi a e (p_a(x,t) - p(x,t)) - (I/\nu) \frac{\partial^2 p(x,t)}{\partial^2 x} - \dot{p}(x,t) A / (RT) = 0.$$

This equation describes the hose system driven by the atmospheric pressure along its length. We transform from the time-length domain, (x,t) , to the frequency and wavenumber domain, (ω, κ) ,

$$p(x,t) = \iint \hat{p}(\omega, \kappa) \exp(-i\omega t) \exp(-i\kappa x) d\omega d\kappa.$$

We can write the solution in the frequency-wavenumber domain,

$$\hat{p}(\omega, x) = \frac{I}{(1 + i\omega/\omega_0 + (\frac{\kappa}{\kappa_0})^2)} \hat{p}_a(\omega, \kappa),$$

$$\tilde{p}(\omega, x) = \int \frac{I}{(1 + i\omega/\omega_0 + (\frac{\kappa}{\kappa_0})^2)} \hat{p}_a(\omega, \kappa) \exp(-i\kappa x) d\kappa.$$

Now we observe that a far-field signal has the form $\hat{p}_a(\omega, \kappa) = \delta(\kappa) \tilde{p}_s(\omega)$, so the signal pressure in the hose is simply

$$\tilde{p}_{signal}(\omega) = \frac{1}{(1 + i\omega/\omega_0)} \tilde{p}_s(\omega).$$

The typical soaker hose has a characteristic time constant, $\tau_0 = 2\pi/\omega_0 = 2\pi a/(2RTe) < 0.2$ seconds, so the pressure signal inside the hose is a faithful representation of the signal outside the hose for infrasound frequencies of interest. This characteristic time is determined by the permeability of the hose. A very permeable hose has a short time constant while an impermeable hose has a long time constant. If we write the atmospheric noise as $\hat{p}_a(\omega, x) = \hat{p}_n(\omega, \kappa)$ then the observed noise signal is given by a Fourier integral over the wavenumber spectrum of the atmospheric noise,

$$\tilde{p}_{noise}(\omega, x) = \int \frac{I}{(1 + i\omega/\omega_0 + (\frac{\kappa}{\kappa_0})^2)} \hat{p}_n(\omega, \kappa) \exp(-i\kappa x) d\kappa,$$

This integral in general cannot be evaluated in closed analytic form; however, by inspection we can note several interesting features. The incoherent atmospheric wavenumbers

are attenuated proportional to $\left(\frac{\kappa}{\kappa_0}\right)^2$ where $\kappa_0^2 = 2\pi a e \nu = 4\pi A \nu / (RT) / \tau_0 = (2\pi / \lambda_0)^2$ is the characteristic wavenumber for the hose. The smaller the characteristic wavenumber, the more attenuated will be the incoherent wavenumbers of the noise field. Note that the characteristic wavenumber for the hose is inversely proportional to the characteristic time constant. Therefore, a long time constant means more noise attenuation for a fixed length of hose. Typical soaker hoses have characteristic lengths, λ_0 , of about 50-200 meters, but we have found that time constants and hence characteristic lengths and the potential noise reduction change with time as the hose ages.

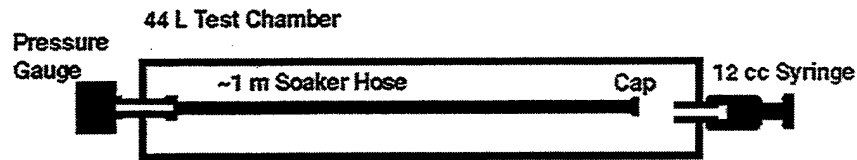


Figure 44. A simple and inexpensive calibration configuration.

The diagram above (Figure 44) shows an experimental setup for measuring time constants of a soaker hose. The soaker hose is placed in the 44 Liter volume test chamber. The test chamber volume is then altered with a 12 cc step function volume decrease, producing a change in pressure of about 300 microbars. Pressure in the soaker hose is recorded using a differential pressure gauge (microbaragraph). The experiment is repeated with different lengths of hose and different amplitude step functions to test for linearity. Pressure transients measured with this setup are shown in Figure 45 for a virgin soaker hose and the same brand of hose left outside for six months during a typical San Diego winter. The time constant for this aged hose has decreased by nearly a factor of two. Hence, noise reduction will have decreased by nearly the same amount.

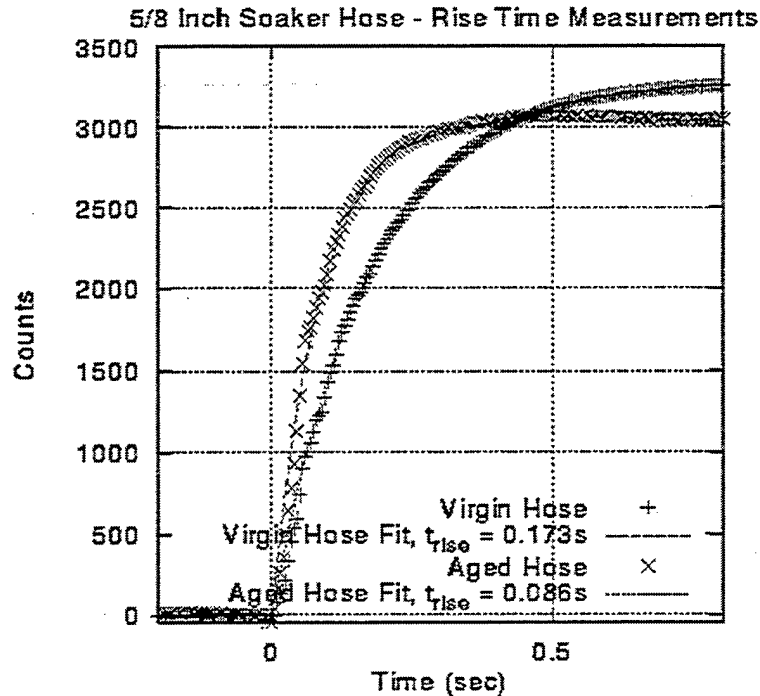


Figure 45. Shows rise time calibration of two 2.082 m long hoses. The "aged" hose had been exposed to the elements for about 6 months during a typical San Diego winter. The rise time and hence the characteristic length of the aged hose is about 50% that of the virgin hose.

Other diagnostic tests are possible for hose systems. The diagram below (Figure 46) shows one such simple test. The results are shown for two identical lengths (about 10 m) of virgin and aged soaker hose (Figure 47). The change in response of the two hoses is clearly evident. In particular, the aged hose transmits nearly half of the pressure amplitude injected compared to the virgin hose. This again demonstrates the importance of controlling permeability of the hose system. This experimental test setup is not as easily analyzed as the previously described arrangement, but it is diagnostic. There is a tendency for a damped Helmholtz oscillation to occur. With shorter lengths of hose this Helmholtz oscillator can be used to measure other properties of the hose such as the flow resistance (damping).

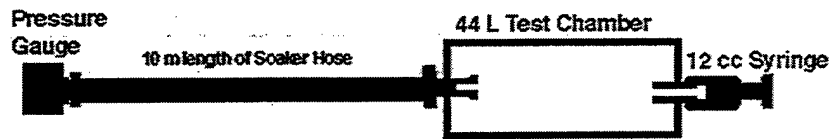


Figure 46. A simple, inexpensive diagnostic configuration. The analysis is not as simple, but the test is sensitive to both the time and length constants of the permeable hose.

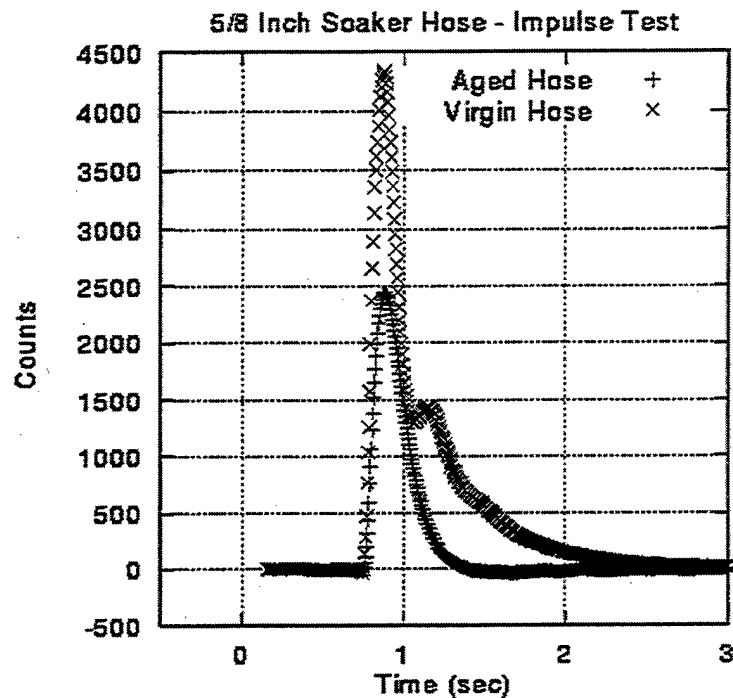


Figure 47. Two short sections of 5/8" permeable hose were tested using the end-on test geometry described in the text. The virgin sample shows a longer time constant and a higher transmittance than the hose exposed to the elements for about 6 months. Increased permeability of the aged hose has shortened the characteristic length and hence the transmittance of the hose by about a factor of 2 at long periods. A small Helmholtz oscillation is evident in the virgin hose but was not excited under identical condition for the aged hose.

4.4 Analysis of a Helmholtz Oscillator

If a manifold is connected to a short non-permeable hose and a step function in pressure is applied to the manifold, it is possible that a Helmholtz oscillator may be set up. This condition occurs when the slug of air within the hose protrudes into the reservoir without immediate mixing and the reservoir acts like a spring. The slug of air acts as a mass connected to the spring and a damped simple harmonic oscillator is set in motion. The viscous flow of air back and forth in the hose causes damping proportional to the flow velocity and the damped simple harmonic oscillator can be modeled to "measure" the damping constants used in the previous analysis.

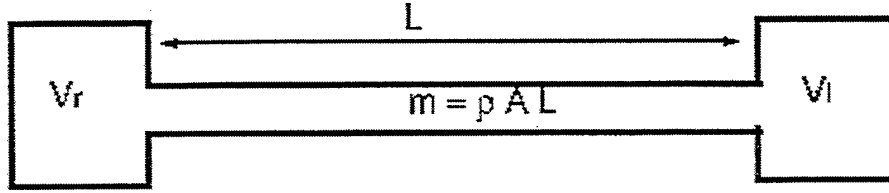


Figure 48. Simple diagram of the principal part of a two-ended Helmholtz oscillator.

The geometry of the oscillator is shown above (Figure 48). The air mass in the length of hose is given by $m = \rho AL$. The displacement of the air mass in the x direction is $u(t)$, and we write Newton's first law,

$$m\ddot{u} = \rho AL\ddot{u} = -L\zeta\dot{u} + A(P_l - P_r),$$

where P_r and P_l are the right and left manifold pressures. If the slug of air protrudes into the manifold with displacement u , and does not mix with the air in the manifold, then the effective volume of the right and left manifolds is $V_r = V_{or} - Au$ and $V_l = V_{ol} + Au$, where V_{or} and V_{ol} are the original right and left manifold volumes. The right and left manifold pressures are given by $\frac{\delta P_r}{P_0} = \frac{\delta V_r}{V_{or}}$ and $\frac{\delta P_l}{P_0} = \frac{\delta V_l}{V_{ol}}$. With some algebra, we have the equation for a simple harmonic oscillator,

$$\rho A L \ddot{u} = L\zeta\dot{u} + A(P_l - P_r) = L\zeta\dot{u} - A^2 P_0 u \left(\frac{1}{V_{or}} + \frac{1}{V_{ol}} \right),$$

$$\ddot{u} = \frac{\zeta}{A\rho} \dot{u} - \frac{AP_0}{L\rho} \left(\frac{1}{V_{or}} + \frac{1}{V_{ol}} \right) u = -\nu \dot{u} - \frac{ART}{L} \left(\frac{1}{V_{or}} + \frac{1}{V_{ol}} \right) u,$$

with natural frequency $\omega_0 = \sqrt{ART(1/V_{or} + 1/V_{ol})/L} = \sqrt{A^2 P_0 (1/V_{or} + 1/V_{ol})/m}$ and damping constant $\beta = \nu A/2 = \zeta/(2A\rho)$. The natural period is proportional to the square root of the manifold volumes and the square root of the hose length. It is desirable to keep manifold volumes small and hence keep parasitic Helmholtz oscillator frequencies in the hose array above the infrasound frequencies of interest. Likewise, it is desirable to

avoid large changes in the cross sectional area of the operational hose-manifold system to avoid the Helmholtz instability. If we assume Poiseuille flow in the hose then the damping constant only depends upon air viscosity, air density, and hose radius, $\beta = \frac{4\eta}{\rho a^2}$. The damping constant does not depend upon the length of the hose. These relations can be used to determine damping characteristics and hence drag terms as shown in Figure 49 below.

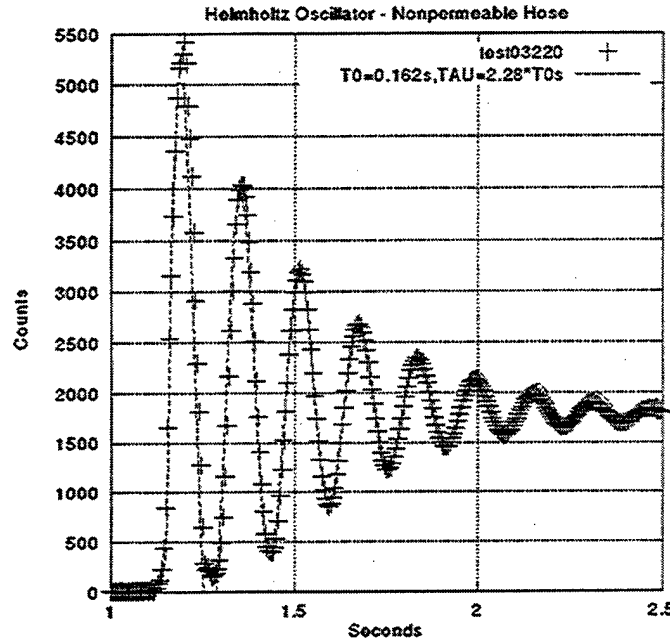


Figure 49. A 0.32 m section of 5/8" non-permeable hose was set up as a Helmholtz oscillator and subjected to a 0.5 millibar step function change in pressure of one manifold. Crosses are data, the dotted line is a damped sinusoidal fit to the data. The damping constant, $\tau = 1/\beta = 0.37 \pm 0.01$ sec, is a measure of flow resistance in the hose and is consistent with Poiseuille flow.

4.5 Finite Difference Modeling, Maxhose

We have developed an implicit finite difference code, **Maxhose**, to simulate the response of a permeable hose and manifold system. Our goal was to model calibration configurations such as those shown in Figures 46 and 47 as well as the response of a system to an arbitrary atmospheric pressure field specified as a function of position and time. We start with the partial differential equation for pressure in the hose as derived above,

$$\dot{p}(x,t) = \left(\frac{RT}{A} \right) 2\pi a e (p_a(x,t)) - p(x,t) - \left(\frac{RT}{Av} \right) \frac{\partial^2 p(x,t)}{\partial x^2}$$

and define $c1 = (RT/Av)$ and $c2 = (RT/A) 2\pi a e$. We discretize the space and time variables, $x_j = x_{j-1} + dx_j$ and $t_n = t_{n-1} + dt_n$, and define a pressure vector of j 'th hose

elements, $p_j^{(n)}$ for time t_n and $p_j^{(n+1)}$ for time t_{n+1} . Pressure, p_j , is the pressure of the volume between $x_j = x_{j-1} + dx_j$ with cross sectional area $A_j = \pi a_j^2$ and volume $V_j = A_j dx_j$. We follow the Crank-Nicolson implicit method (Smith 1978; Davis 1986) to derive a set of second order finite difference equations for the pressure updates at time step $n+1$ from the pressures at time step n . The system of equations that must be solved is,

$$\begin{aligned} & p_j^{(n+1)} - (c_j^1 dt_n / 2 / dx_j^2) (p_{j+1}^{(n+1)} - 2p_j^{(n+1)} + p_{j-1}^{(n+1)}) \\ & + (c_j^2 dt_n / 2) p_j^{(n+1)} \\ & = \\ & p_j^{(n)} + (c_j^1 dt_n / 2 / dx_j^2) (p_{j+1}^{(n)} - 2p_j^{(n)} + p_{j-1}^{(n)}) - (c_j^2 dt_n / 2) p_j^{(n)} \\ & + (3c_j^2 dt_n / 2) p_j^{(n)} \\ & + (c_j^2 dt_n / 2) (p_{aj}^{(n+1)} + p_{aj}^{(n)} - 2p_j^{(n)}), \text{ for } j = 2, N-1 \end{aligned}$$

where p_j is the pressure inside the j 'th element of the hose and p_{aj} is the atmospheric pressure outside the j 'th element of the hose. Note that $c1$ and $c2$ may depend upon position along the hose and that the spatial differences must be altered if hose elements are not uniform lengths, dx_j . We use second order approximations for the spatial and temporal derivatives. We require two sets of boundary conditions at the ends of the hose at $x_1 = 0$ and $x_N = L$. The first useful boundary condition is a no-flow condition where the spatial pressure derivative is zero. The left-hand side no-flow boundary equation becomes,

$$p_{j+1}^{(n+1)} - p_j^{(n+1)} = 0, \text{ where } j = 1$$

and right-hand side no-flow boundary condition

$$p_{j+1}^{(n+1)} - p_j^{(n+1)} = 0, \text{ where } j = N.$$

The second set of useful boundary conditions are volumetric reservoirs or manifolds at either end of a hose. In the case of multiple hoses, they are connected by manifolds of finite volume. If we assume pressure changes in the manifold are at constant temperature, then we have the relationship $p/(\text{mass}/V) = p/\rho = RT = p_0/\rho_0$ for the manifold. The change in pressure is therefore proportional to the mass flux,

$$\delta p = p \frac{\delta m}{m} = (p/m) q_x dt = (RT/V) dt (1/v) \partial p(x,t) / \partial x.$$

If we have volume reservoirs of volume V_j at $j = 1$ and/or $j = N$, then using the Crank-Nicolson scheme we arrive at the left-hand side boundary condition equation,

$$p_j^{(n+1)} - \left(\frac{RTdt}{2\nu V_j dx_j} \right) (p_{j+1}^{(n+1)} - p_j^{(n+1)}) = p_j^{(n)} + \left(\frac{RTdt}{2\nu V_j dx_j} \right) (p_{j+1}^{(n)} - p_j^{(n)}), \text{ for } j = 1,$$

and the right-hand side boundary condition,

$$p_j^{(n+1)} - \left(\frac{RTdt}{2\nu V_j dx_j} \right) (p_{j+1}^{(n+1)} - p_j^{(n+1)}) = p_j^{(n)} + \left(\frac{RTdt}{2\nu V_j dx_j} \right) (p_{j+1}^{(n)} - p_j^{(n)}), \text{ for } j = N.$$

Equations documented up to this point assume momentum of the gas within the hose is insignificant or inertial forces are not significant. Under some circumstances this may not be the case, so we now derive equations for the velocities, v_j , along the hose. The rate of change of momentum in the x-direction in the hose element of length, dx , may be written,

$$\begin{aligned} \frac{d(mv)}{dt} &= \dot{m}v + m\dot{v} \approx (\rho A dx) \dot{v} \\ &= F_{drag} - A(p(x+dx) - p(x)) \\ &= \zeta dx v - A(p(x+dx) - p(x)) \\ &= -\rho v A^2 v - A(p(x+dx) - p(x)). \end{aligned}$$

We must assume that $\dot{m}v \ll m\dot{v}$ or nonlinear terms (velocity times pressure) will appear in the response of the hose and we have,

$$\dot{v} = v A v - \left(\frac{1}{\rho dx} \right) (p(x+dx) - p(x)).$$

Note that for constant velocity flow with a constant pressure difference along a section of hose we have $\dot{v} = \left(\frac{1}{\nu A \rho dx} \right) (p(x+dx) - p(x))$, and if this corresponds to simple Poiseuille flow, $\nu \rho A = \frac{\pi a^4}{8\eta dx} (p(x+dx) - p(x))$, and the flow resistance constants may be computed from the air viscosity, $\zeta = 8\pi\eta$, $\nu = 8\eta / \pi / \rho / a^4$.

Let $c3 = -Av/dx$ and $c4 = -A/mass = -1/(\rho dx)$. We let the discrete velocity vector, v_j , correspond to the velocities between the hose elements at $x = x_j$ at node j . Therefore, the velocities and pressures constitute a staggered grid. Pressures are defined between x_j and x_{j+1} while the velocities are defined at x_j . Again, we apply the Crank-Nicolson formalism to derive finite difference equations that couple velocities and pressures at time, t_{n+1} , and t_n .

$$\begin{aligned} & \left(1 - \frac{dt_j c 3_j}{2}\right) v_j^{(n+1)} - \frac{dt_j c 4_j}{2} (p_{j+1}^{(n+1)} - p_j^{(n+1)}) = \\ & \left(1 + \frac{dt_j c 3_j}{2}\right) v_j^{(n+1)} + \frac{dt_j c 4_j}{2} (p_{j+1}^{(n+1)} - p_j^{(n)}), \text{ for } j = 2, N-1. \end{aligned}$$

Note the $c4$ coefficients depend upon local mass and therefore they are time dependent and must be updated with each time step using

$$\begin{aligned} \delta m_j &= dt a_j e_j (2p_{ej}^{(n)} - p_j^{(n)} - p_j^{(n+1)}) \\ &+ \left(\frac{dt}{v_j}\right) (p_{j+1}^{(n)} - p_{j-1}^{(n)} + p_{j+1}^{(n+1)} - p_{j-1}^{(n+1)}) / (4dx_j). \end{aligned}$$

For left-hand side no-flow boundary conditions we have, $v_j^{(n+1)} = 0$, for $j = 1$. For right-hand side no-flow boundary conditions we have, $v_j^{(n+1)} = 0$, for $N+1$. If we have no-flow boundary conditions on both ends of the hose, then there are N hose elements (pressures) and $N+1$ nodes (velocities).

If we have a volumetric reservoir at $j = 1$ then the $j = 1$ velocity corresponds to the flow velocity between the reservoir and the first hose element, consistent with our previous pressure boundary condition equations, we have,

$$\begin{aligned} & \left(1 - \frac{dt c 3_j}{2}\right) v_j^{(n+1)} - \frac{dt c 4_j}{2} (p_{j+1}^{(n+1)} - p_j^{(n+1)}) = \\ & \left(1 + \frac{dt c 3_j}{2}\right) v_j^{(n+1)} + \frac{dt c 4_j}{2} (p_{j+1}^{(n+1)} - p_j^{(n)}), \text{ for } j = 1. \end{aligned}$$

If we have a volumetric reservoir at $j = N$, then the $j = N-1$ velocity is between the last ($N-1$) hose element and the reservoir. The right-hand side boundary condition becomes,

$$\begin{aligned} & \left(1 - \frac{dt c 3_{j-1}}{2}\right) v_{j-1}^{(n+1)} - \frac{dt c 4_{j-1}}{2} (p_j^{(n+1)} - p_{j-1}^{(n+1)}) = \\ & \left(1 + \frac{dt c 3_{j-1}}{2}\right) v_{j-1}^{(n+1)} + \frac{dt c 4_{j-1}}{2} (p_j^{(n)} - p_{j-1}^{(n)}), \text{ for } j = N. \end{aligned}$$

For both right-hand and left-hand side no-flow boundary conditions there are N pressure equations and $N+1$ velocity equations. For both right-hand side and left-hand side volumetric reservoirs there are N pressure equations and $N-1$ velocity equations. At each $(n+1)$ time step, linear equations are solved, $\mathbf{A}\mathbf{u}^{(n+1)} = \mathbf{B}\mathbf{u}^{(n)} + \mathbf{C}(\mathbf{w}^{(n)} - \mathbf{u}^{(n)}) = \mathbf{b}^{(n)}$, for the new vector, $\mathbf{u}^{(n+1)}$, of pressures and velocities $\mathbf{W}^{(n)}$ is the vector of atmospheric pressures along the hose. We construct the pressure-velocity vector components; $u_{2j} = p_j$, $u_{2j-1} = v_j$, and $w_{2j} = p_{aj}$, $w_{2j-1} = 0$, for $j = 1$ to N . $C_{(2j-1),(2j-1)} = 0$ and $C_{2j,2j} = 1$ for $j = 1, N$. The \mathbf{A} and \mathbf{B} matrices are very sparse but not necessarily banded when multiple coupled hoses are

considered, therefore a general sparse matrix linear equation solver is used rather than a solver that assumes a strictly banded system.

4.6 Stability Conditions

While the Crank-Nicolson implicit scheme is generally stable regardless of time step size, we address one possible source of instability. Negative values of pressure and mass are valid solutions to the equations but physically meaningless. Mass and pressure are explicitly positive quantities; therefore, we wish to avoid large changes in the mass of any hose or manifold element, $|\delta m| < m$ at any given time step. The lateral mass flux across each node should be small compared to the mass within an element during a time step,

$$|dm| = \left| dt \frac{\partial p}{\partial x} \left(\frac{-1}{v} \right) \right| < p \text{ vol} / RT = p dx A / RT,$$

which leads to a restriction on the time step, dt , for each node,

$$dt < \frac{p dx A v}{RT |\partial p / \partial x|} \approx \frac{p_j}{|p_j - p_{j-1}|} \left(\frac{dx^2 A_j v_j}{RT} \right) = \frac{p_j}{|p_j - p_{j-1}|} \left(\pi \tau_{0j} \frac{dx^2}{\lambda_{0j}^2} \right), \text{ for all } j.$$

Likewise, the change in mass of the right- and left-hand volumetric reservoirs should remain small compared to the mass of these reservoirs as well as the mass of their adjacent hose elements. The conditions for these restrictions on dt are easily derived. We write them here for completeness,

$$dt < \frac{v_{\min} (p_{j+1} dx_{j+1} A_{j+1} p_j V_{0l})}{|p_j - p_{j-1}|}, \text{ for } j = 1,$$

and

$$dt < \frac{v_{\min} (p_{j-1} dx_{j-1} A_{j-1} p_j V_{0r})}{RT |p_j - p_{j-1}|}, \text{ for } j = N,$$

The diffusive flows into or out of the hose elements must also remain small for each time step,

$$|dm| = |dt 2\pi a e (p_a - p) dx| < p \text{ vol} / RT = p dx A / RT,$$

$$dt < \frac{p_j}{|p_a - p_{j-1}|} \left(\frac{A_j}{RT 2\pi a_j e_j} \right) = \frac{p_j}{|p_a - p_{j-1}|} \left(\frac{\tau_{0j}}{2\pi} \right) \text{ for all } j \text{ with } e_j > 0.$$

4.7 Hose Calibration Simulation

Figure 50 shows three **Maxhose** simulations of the calibration test configuration diagrammed in Figure 44 compared to virgin hose data from Figure 6. A proper analysis of the calibration data requires that the pressure gauge manifold be included in the response. When the manifolds are included in the simulation, the value of $\tau_0 = 0.10$ sec. fits the data very well.

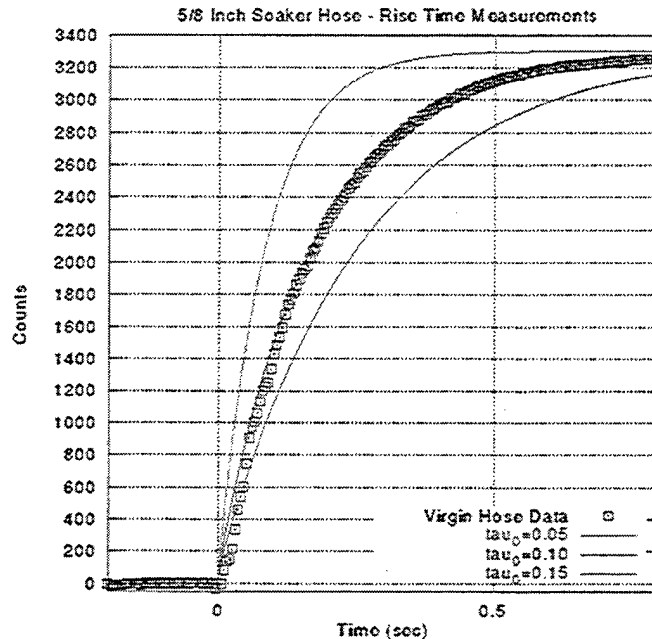


Figure 50. Comparison of data and Maxhose finite difference simulation of the calibration test configuration of Figure 44.

4.8 Finite Difference Simulations of Wind Noise Response

We have demonstrated the use of the finite difference code, **Maxhose**, to model the hose response from atmospheric wind noise. An atmospheric pressure history is specified as a function of time and position along the hose, $p_a(t,x)$, and the pressure inside the hose is computed. Figure 51 shows the results for $p_a(t,x)$ specified as white noise on a 50 m hose with characteristic time of 0.01 second and a characteristic length of 100 m. While this is not a realistic wind noise situation, it illustrates several aspects of the permeable hose response. The numerical experiment was repeated for several hose lengths and the predicted noise reductions are summarized in Figure 52. RMS noise levels are reduced by nearly a factor 40 in the middle of a hose that is longer than 1/2 the characteristic length. Noise reduction saturates at about 1/2 the characteristic length. For such a hose under white noise conditions, noise levels at the end of the hose are roughly 30% higher than the levels in the center of the hose.

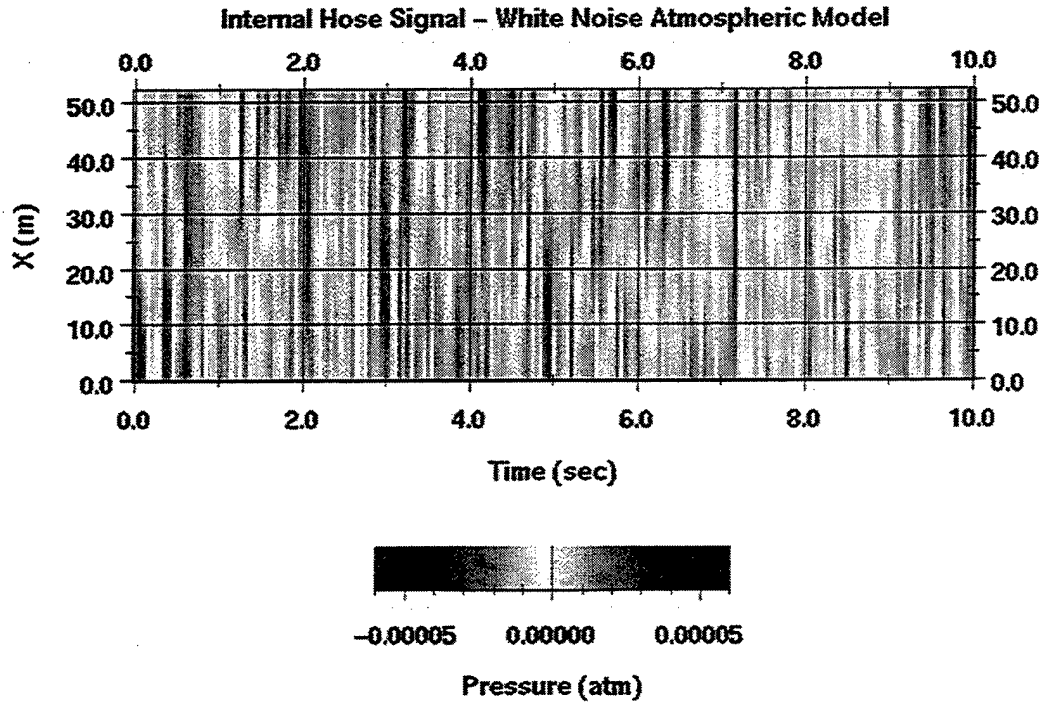


Figure 51. Pressure variation in the hose as a function of time (seconds) and position (X in meters) for random white noise pressure fluctuations in the atmosphere. Note that the hose smooths out the pressures along the hose.

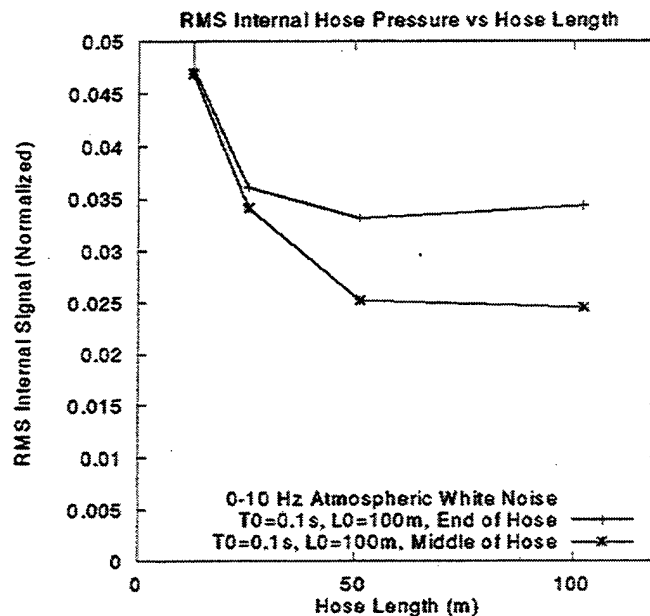


Figure 52. RMS pressure fluctuations normalized to external atmospheric RMS fluctuations at the end of the hose and in the middle of the hose versus different hose lengths for a fixed characteristic length hose. Note that noise reduction is best in the middle of the hose.

Under more realistic wind conditions, atmospheric pressure fluctuations exhibit spatial correlation. Given an arbitrary correlation function or power spectrum we can synthesize a realization of the atmospheric noise. In the absence of a deterministic wind model, we have postulated that $p_a(t,x)$ appears as Brownian or fractal noise with a power spectrum that is inversely proportional to frequency and wavenumber, f^{-a} and k^{-b} , where a and b are specified constants. Figure 53 shows the results of such a Monte Carlo simulation with $a = b = 2$. The same hose characteristics were used as in previous simulations. An ambient atmospheric pressure noise source is shown with a power spectrum approximately proportional to k^{-2} and f^{-2} is shown on the left and the internal hose pressure fluctuations are shown on the right. Note that the hose has spatially averaged the pressure field. High frequencies and spatial wavenumbers have been reduced. However, low spatial wavenumbers are still evident in the internal hose signal (Figure 54).

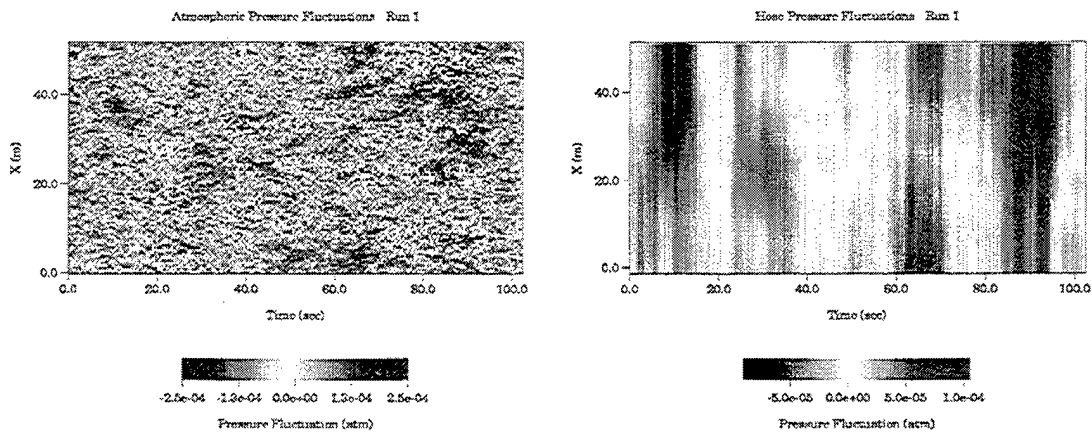


Figure 53. An atmospheric pressure history as a function of space and time on the left and the resulting pressure fluctuation signal in the hose on the right. The 50 m hose reduces the atmospheric noise by averaging it over the length of the hose with characteristic length of 100 m.

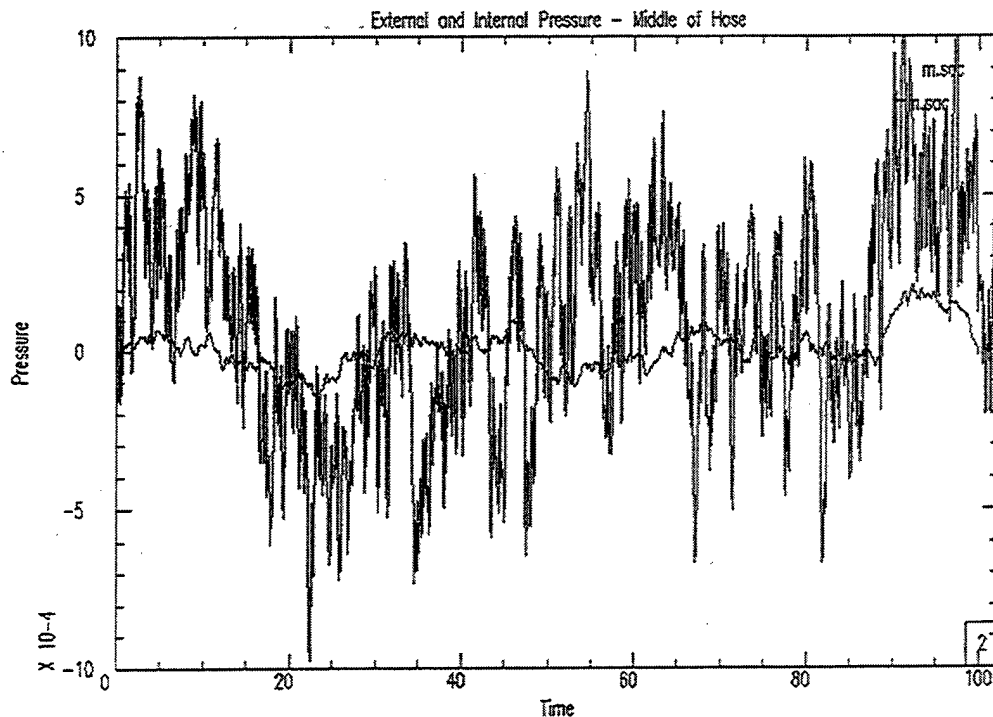


Figure 54. Pressure fluctuations inside and outside the middle of the hose simulation of Figure 53.

4.9 Conclusions

Noise reduction is critical for the successful utilization of microbarograph arrays in a future CTBT system. Current plans for the IMS anticipate signal to noise increases from multiple hose arrays on the order of 100 for common wind conditions.

We present an analysis of the partial differential equations that govern the response of pressure within a permeable hose to external atmospheric pressures. We show that a hose may be characterized by a time constant and characteristic length. The characteristic time constant is determined by the permeability of the hose. The characteristic length is determined by the permeability of the hose and flow resistance along the hose. Methods for measurement of the time and length constant are proposed.

Noise signals in the hose will be attenuated for pressure fluctuations in the atmosphere with wavelengths shorter than the characteristic hose length. Infrasound signals with apparent wavelengths longer than the hose will not be so attenuated and the hose affords a net signal-to-noise ratio gain. Control of permeability of the hose is critical to the signal-to-noise ratio gains that can be realized. Measurements of the time constants of hoses have shown that the permeability can change by a factor of two due to natural weathering of a hose. Methods must be devised to protect hoses in the field and to diagnose hose degradation in operational systems.

Conversion of the partial differential equations to a finite difference program, **Maxhose**, is described. **Maxhose** simulates hose pressure response to an arbitrary atmospheric pressure defined as a function of time and position along the hose. This second order implicit Crank-Nicholson code runs on UNIX workstations and Windows 95 computers. Results are shown for simple calibration configurations and for two Monte Carlo realizations of wind noise. If wind noise is uncorrelated in space and time, then noise reduction for a single hose is predicted to be about a factor of 40 and maximized in the center of a hose at least as long as 1/2 the characteristic length. Noise reduction for a single hose in the case of fractal noise is somewhat less and depends critically upon the details of the atmospheric turbulence spectrum. **Maxhose** can be extended to simulate multiple hose arrays and wind noise with arbitrary correlation structures in space and time. Analysis of this kind coupled with an understanding of wind noise correlation structures will prove useful in understanding the potential for permeable hose noise reduction.

4.10 Acknowledgments

We wish to thank David Harkrider, Robert Blandford, Dean Clauter, Chris Hayward, Mike Sorrels, and Steven Peyton for their helpful discussions on infrasound propagation and hose physics.

4.11 References

- Blandford, R. R. and D. A. Clauter (1995), "Capability Estimation Of Infrasound Networks," AFTAC Technical Report, July.
- Burridge, R. (1971), "The Acoustics of Pipe Arrays," *Geop. J. Roy. Astr. Soc.* 26, 53-69.
- Cook, R. K., Bedard, A. J. (1971), "On the Measurement of Infrasound," *Geop. J. Roy. Astr. Soc.*, 26, 5-11.
- Daniels, F. B. (1959), "Noise Reducing Line Microphone for Frequencies Below 1 c/s," *J. Acoust. Soc. Am.*, 31, 529.
- Davis, J. L. (1986), *Finite Difference Methods in Dynamics of Continuous Media*, MacMillan Publishing Co., 238 pp.
- Grover, F. H. (1971), "Experimental Noise Reducers for an Active Microbarograph," *Geop. J. Roy. Astr. Soc.*, 26, 41-52.
- Mack, H. and E. A. Flinn (1971), "Analysis of the Spatial Coherence of Short-Period Acoustic-Gravity Waves in the Atmosphere," *Geop. J. Roy. Astr. Soc.*, 26, 255-269.

THOMAS AHRENS
SEISMOLOGICAL LABORATORY 252-21
CALIFORNIA INST. OF TECHNOLOGY
PASADENA, CA 91125

AIR FORCE RESEARCH LABORATORY
ATTN: VSOE
29 RANDOLPH ROAD
HANS COM AFB, MA 01731-3010
(2 COPIES)

AIR FORCE RESEARCH LABORATORY
ATTN: RESEARCH LIBRARY/TL
5 WRIGHT STREET
HANS COM AFB, MA 01731-3004

AIR FORCE RESEARCH LABORATORY
ATTN: AFRL/SUL
3550 ABERDEEN AVE SE
KIRTLAND AFB, NM 87117-5776
(2 COPIES)

RALPH ALEWINE
NTPO
1901 N. MOORE STREET, SUITE 609
ARLINGTON, VA 22209

MUAWIA BARAZANGI
INSTOC
3126 SNEE HALL
CORNELL UNIVERSITY
ITHACA, NY 14853

T.G. BARKER
MAXWELL TECHNOLOGIES
8888 BALBOA AVE.
SAN DIEGO, CA 92123-1506

DOUGLAS BAUMGARDT
ENSCO INC.
5400 PORT ROYAL ROAD
SPRINGFIELD, VA 22151

THERON J. BENNETT
MAXWELL TECHNOLOGIES
11800 SUNRISE VALLEY DRIVE, STE 1212
RESTON, VA 22091

WILLIAM BENSON
NAS/COS
ROOM HA372
2001 WISCONSIN AVE. NW
WASHINGTON DC 20007

JONATHAN BERGER
UNIVERSITY OF CA, SAN DIEGO
SCRIPPS INST. OF OCEANOGRAPHY
IGPP, 0225
9500 GILMAN DRIVE
LA JOLLA, CA 92093-0225

ROBERT BLANDFORD
AFTAC
1300 N. 17TH STREET
SUITE 1450
ARLINGTON, VA 22209-2308

LESLIE A. CASEY
DEPT. OF ENERGY/NN-20
1000 INDEPENDENCE AVE. SW
WASHINGTON DC 20585-0420

CENTER FOR MONITORING RESEARCH
ATTN: LIBRARIAN
1300 N. 17th STREET, SUITE 1450
ARLINGTON, VA 22209

ANTON DAINTY
HQ DSWA/PMA
6801 TELEGRAPH ROAD
ALEXANDRIA, VA 22310-3398

CATHERINE DE GROOT-HEDLIN
UNIV. OF CALIFORNIA, SAN DIEGO
INST. OF GEOP. & PLANETARY PHYSICS
8604 LA JOLLA SHORES DRIVE
SAN DIEGO, CA 92093

DTIC
8725 JOHN J. KINGMAN ROAD
FT BELVOIR, VA 22060-6218 (2 COPIES)

DIANE DOSER
DEPT OF GEOLOGICAL SCIENCES
THE UNIVERSITY OF TEXAS AT EL PASO
EL PASO, TX 79968

MARK D. FISK
MISSION RESEARCH CORPORATION
735 STATE STREET
P.O. DRAWER 719
SANTA BARBARA, CA 93102-0719

LORI GRANT
MULTIMAX, INC.
311C FOREST AVE. SUITE 3
PACIFIC GROVE, CA 93950

HENRY GRAY
SMU STATISTICS DEPARTMENT
P.O. BOX 750302
DALLAS, TX 75275-0302

I. N. GUPTA
MULTIMAX, INC.
1441 MCCORMICK DRIVE
LARGO, MD 20774

DAVID HARKRIDER
BOSTON COLLEGE
INSTITUTE FOR SPACE RESEARCH
140 COMMONWEALTH AVENUE
CHESTNUT HILL, MA 02167

THOMAS HEARN
NEW MEXICO STATE UNIVERSITY
DEPARTMENT OF PHYSICS
LAS CRUCES, NM 88003

MICHAEL HEDLIN
UNIV. OF CALIFORNIA, SAN DIEGO
SCRIPPS INST. OF OCEANOGRAPHY
IGPP, 0225
9500 GILMAN DRIVE
LA JOLLA, CA 92093-0225

DONALD HELMBERGER
CALIFORNIA INST. OF TECHNOLOGY
DIV. OF GEOL. & PLANETARY SCIENCES
SEISMOLOGICAL LABORATORY
PASADENA, CA 91125

EUGENE HERRIN
SOUTHERN METHODIST UNIVERSITY
DEPARTMENT OF GEOLOGICAL
SCIENCES
DALLAS, TX 75275-0395

ROBERT HERRMANN
ST. LOUIS UNIVERSITY
DEPT OF EARTH & ATMOS. SCIENCES
3507 LACLEDE AVENUE
ST. LOUIS, MO 63103

VINDELL HSU
HQ/AFTAC/TTR
1030 S. HIGHWAY A1A
PATRICK AFB, FL 32925-3002

RONG-SONG JIH
HQ DSWA/PMA
6801 TELEGRAPH ROAD
ALEXANDRIA, VA 22310-3398

THOMAS JORDAN
MASS. INST. OF TECHNOLOGY
BLDG 54-918
77 MASSACHUSETTS AVENUE
CAMBRIDGE, MA 02139

LAWRENCE LIVERMORE NAT'L LAB
ATTN: TECHNICAL STAFF (PLS ROUTE)
PO BOX 808, MS L-175
LIVERMORE, CA 94551

LAWRENCE LIVERMORE NAT'L LAB
ATTN: TECHNICAL STAFF (PLS ROUTE)
PO BOX 808, MS L-208
LIVERMORE, CA 94551

LAWRENCE LIVERMORE NAT'L LAB
ATTN: TECHNICAL STAFF (PLS ROUTE)
PO BOX 808, MS L-202
LIVERMORE, CA 94551

LAWRENCE LIVERMORE NAT'L LAB
ATTN: TECHNICAL STAFF (PLS ROUTE)
PO BOX 808, MS L-195
LIVERMORE, CA 94551

LAWRENCE LIVERMORE NAT'L LAB
ATTN: TECHNICAL STAFF (PLS ROUTE)
PO BOX 808, MS L-205
LIVERMORE, CA 94551

LAWRENCE LIVERMORE NAT'L LAB
ATTN: TECHNICAL STAFF (PLS ROUTE)
PO BOX 808, MS L-200
LIVERMORE, CA 94551

LAWRENCE LIVERMORE NAT'L LAB
ATTN: TECHNICAL STAFF (PLS ROUTE)
PO BOX 808, MS L-221
LIVERMORE, CA 94551

THORNE LAY
UNIV. OF CALIFORNIA, SANTA CRUZ
EARTH SCIENCES DEPARTMENT
EARTH & MARINE SCIENCE BUILDING
SANTA CRUZ, CA 95064

ANATOLI L. LEVSHIN
DEPARTMENT OF PHYSICS
UNIVERSITY OF COLORADO
CAMPUS BOX 390
BOULDER, CO 80309-0309

JAMES LEWKOWICZ
WESTON GEOPHYSICAL CORP.
325 WEST MAIN STREET
NORTHBORO, MA 01532

LOS ALAMOS NATIONAL LABORATORY
ATTN: TECHNICAL STAFF (PLS ROUTE)
PO BOX 1663, MS F659
LOS ALAMOS, NM 87545

LOS ALAMOS NATIONAL LABORATORY
ATTN: TECHNICAL STAFF (PLS ROUTE)
PO BOX 1663, MS F665
LOS ALAMOS, NM 87545

LOS ALAMOS NATIONAL LABORATORY
ATTN: TECHNICAL STAFF (PLS ROUTE)
PO BOX 1663, MS C335
LOS ALAMOS, NM 87545

GARY MCCARTOR
SOUTHERN METHODIST UNIVERSITY
DEPARTMENT OF PHYSICS
DALLAS, TX 75275-0395

KEITH MCLAUGHLIN
CENTER FOR MONITORING RESEARCH
SAIC
1300 N. 17TH STREET, SUITE 1450
ARLINGTON, VA 22209

BRIAN MITCHELL
DEPT OF EARTH & ATMOS. SCIENCES
ST. LOUIS UNIVERSITY
3507 LACLEDE AVENUE
ST. LOUIS, MO 63103

RICHARD MORROW
USACDA/IVI
320 21ST STREET, N.W.
WASHINGTON DC 20451

JOHN MURPHY
MAXWELL TECHNOLOGIES
11800 SUNRISE VALLEY DRIVE, STE 1212
RESTON, VA 22091

JAMES NI
NEW MEXICO STATE UNIVERSITY
DEPARTMENT OF PHYSICS
LAS CRUCES, NM 88003

ROBERT NORTH
CENTER FOR MONITORING RESEARCH
1300 N. 17th STREET, SUITE 1450
ARLINGTON, VA 22209

OFFICE OF THE SECRETARY OF DEFENSE
DDR&E
WASHINGTON DC 20330

JOHN ORCUTT
INST. OF GEOPH. & PLANETARY PHYSICS
UNIV. OF CALIFORNIA, SAN DIEGO
LA JOLLA, CA 92093

PACIFIC NORTHWEST NAT'L LAB
ATTN: TECHNICAL STAFF (PLS ROUTE)
PO BOX 999, MS K6-48
RICHLAND, WA 99352

PACIFIC NORTHWEST NAT'L LAB
ATTN: TECHNICAL STAFF (PLS ROUTE)
PO BOX 999, MS K6-40
RICHLAND, WA 99352

PACIFIC NORTHWEST NAT'L LAB
ATTN: TECHNICAL STAFF (PLS ROUTE)
PO BOX 999, MS K6-84
RICHLAND, WA 99352

PACIFIC NORTHWEST NAT'L LAB
ATTN: TECHNICAL STAFF (PLS ROUTE)
PO BOX 999, MS K5-12
RICHLAND, WA 99352

FRANK PILOTTE
HQ AFTAC/TT
1030 S. HIGHWAY A1A
PATRICK AFB, FL 32925-3002

KEITH PRIESTLEY
DEPARTMENT OF EARTH SCIENCES
UNIVERSITY OF CAMBRIDGE
MADINGLEY RISE, MADINGLEY ROAD
CAMBRIDGE, CB3 0EZ UK

JAY PULLI
BBN SYSTEMS AND TECHNOLOGIES, INC.
1300 NORTH 17TH STREET
ROSSLYN, VA 22209

DELAINE REITER
AFRL/VSOE (SENCOM)
29 RANDOLPH ROAD
HANSKOM AFB, MA 01731-3010

PAUL RICHARDS
COLUMBIA UNIVERSITY
LAMONT-DOHERTY EARTH OBSERV.
PALISADES, NY 10964

MICHAEL RITZWOLLER
DEPARTMENT OF PHYSICS
UNIVERSITY OF COLORADO
CAMPUS BOX 390
BOULDER, CO 80309-0309

DAVID RUSSELL
HQ AFTAC/TTR
1030 SOUTH HIGHWAY A1A
PATRICK AFB, FL 32925-3002

CHANDAN SAIKIA
WOODWARD-CLYDE FED. SERVICES
566 EL DORADO ST., SUITE 100
PASADENA, CA 91101-2560

SANDIA NATIONAL LABORATORY
ATTN: TECHNICAL STAFF (PLS ROUTE)
DEPT. 5704
MS 0979, PO BOX 5800
ALBUQUERQUE, NM 87185-0979

SANDIA NATIONAL LABORATORY
ATTN: TECHNICAL STAFF (PLS ROUTE)
DEPT. 9311
MS 1159, PO BOX 5800
ALBUQUERQUE, NM 87185-1159

SANDIA NATIONAL LABORATORY
ATTN: TECHNICAL STAFF (PLS ROUTE)
DEPT. 5704
MS 0655, PO BOX 5800
ALBUQUERQUE, NM 87185-0655

SANDIA NATIONAL LABORATORY
ATTN: TECHNICAL STAFF (PLS ROUTE)
DEPT. 5736
MS 0655, PO BOX 5800
ALBUQUERQUE, NM 87185-0655

THOMAS SERENO, JR.
SAIC
10260 CAMPUS POINT DRIVE
SAN DIEGO, CA 92121

AVI SHAPIRA
SEISMOLOGY DIVISION
IPRG
P.O.B. 2286
NOLON 58122 ISRAEL

ROBERT SHUMWAY
410 MRAK HALL
DIVISION OF STATISTICS
UNIVERSITY OF CALIFORNIA
DAVIS, CA 95616-8671

MATTHEW SIBOL
ENSCO, INC.
445 PINEDA CT.
MELBOURNE, FL 32940

DAVID SIMPSON
IRIS
1200 NEW YORK AVE., NW
SUITE 800
WASHINGTON DC 20005

JEFFRY STEVENS
MAXWELL TECHNOLOGIES
8888 BALBOA AVE.
SAN DIEGO, CA 92123-1506

BRIAN SULLIVAN
BOSTON COLLEGE
INSITUTE FOR SPACE RESEARCH
140 COMMONWEALTH AVENUE
CHESTNUT HILL, MA 02167

TACTEC
BATTELLE MEMORIAL INSTITUTE
505 KING AVENUE
COLUMBUS, OH 43201 (FINAL REPORT)

NAFI TOKSOZ
EARTH RESOURCES LABORATORY, M.I.T.
42 CARLTON STREET, E34-440
CAMBRIDGE, MA 02142

LAWRENCE TURNBULL
ACIS
DCI/ACIS
WASHINGTON DC 20505

GREG VAN DER VINK
IRIS
1200 NEW YORK AVE., NW
SUITE 800
WASHINGTON DC 20005

FRANK VERNON
UNIV. OF CALIFORNIA, SAN DIEGO
SCRIPPS INST. OF OCEANOGRAPHY
IGPP, 0225
9500 GILMAN DRIVE
LA JOLLA, CA 92093-0225

TERRY WALLACE
UNIVERSITY OF ARIZONA
DEPARTMENT OF GEOSCIENCES
BUILDING #77
TUCSON, AZ 85721

JILL WARREN
LOS ALAMOS NATIONAL LABORATORY
GROUP NIS-8
P.O. BOX 1663
LOS ALAMOS, NM 87545 (5 COPIES)

DANIEL WEILL
NSF
EAR-785
4201 WILSON BLVD., ROOM 785
ARLINGTON, VA 22230

RU SHAN WU
UNIV. OF CALIFORNIA SANTA CRUZ
EARTH SCIENCES DEPT.
1156 HIGH STREET
SANTA CRUZ, CA 95064

JIAKANG XIE
COLUMBIA UNIVERSITY
LAMONT DOHERTY EARTH OBSERV.
ROUTE 9W
PALISADES, NY 10964

JAMES E. ZOLLWEG
BOISE STATE UNIVERSITY
GEOSCIENCES DEPT.
1910 UNIVERSITY DRIVE
BOISE, ID 83725